

EFFICIENT DEGRADATION-AGNOSTIC IMAGE RESTORATION VIA CHANNEL-WISE FUNCTIONAL DECOMPOSITION AND MANIFOLD REGULARIZATION

Bin Ren^{1,2} Yawei Li³ Xu Zheng⁴ Yuqian Fu⁵ Danda Pani Paudel⁵ Hong Liu^{6*}
Ming-Hsuan Yang⁷ Luc Van Gool⁵ Nicu Sebe²

¹Mohamed bin Zayed University of Artificial Intelligence ²University of Trento ³ETH Zürich

⁴HKUST (GZ) ⁵INSAIT, Sofia University “St. Kliment Ohridski”

⁶Peking University ⁷University of California, Merced

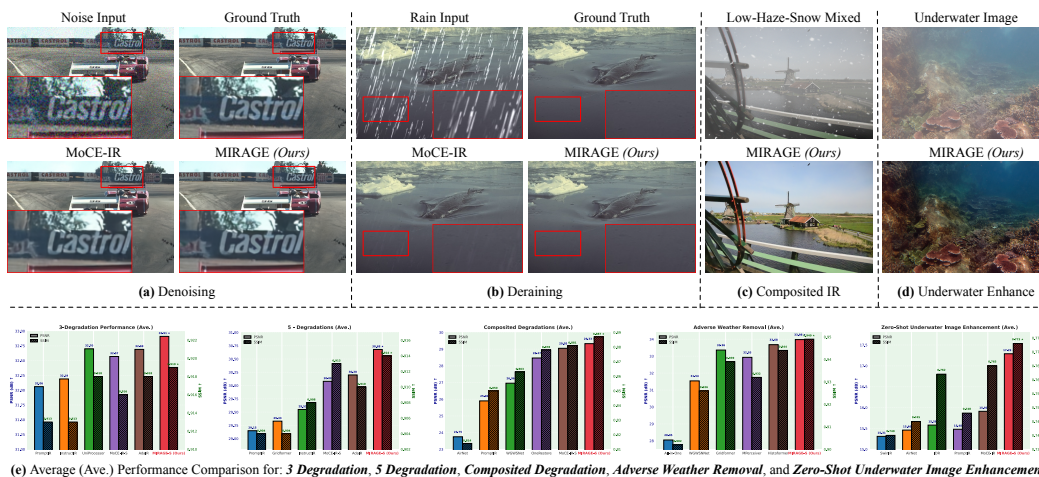


Figure 1: (a)-(d): Visual comparison for Denoising, Deraining, Compositd Degradations (low-light, haze, and snow), and underwater image enhancement. (e): The average PSNR and SSIM comparison across 4 challenging all-in-one and 1 zero-shot settings (Please zoom in for a better view).

ABSTRACT

Degradation-agnostic image restoration aims to handle diverse corruptions with one unified model, but faces fundamental challenges in balancing efficiency and performance across different degradation types. Existing approaches either sacrifice efficiency for versatility or fail to capture the distinct representational requirements of various degradations. We present MIRAGE, an efficient framework that addresses these challenges through two key innovations. First, we propose a channel-wise functional decomposition that systematically repurposes channel redundancy in attention mechanisms by assigning CNN, attention, and MLP branches to handle local textures, global context, and channel statistics, respectively. This principled decomposition enables degradation-agnostic learning while achieving superior efficiency-performance trade-offs. Second, we introduce manifold regularization that performs cross-layer contrastive alignment in Symmetric Positive Definite (SPD) space, which empirically improves feature consistency and generalization across degradation types. Extensive experiments demonstrate that MIRAGE achieves state-of-the-art performance with remarkable efficiency, outperforming existing methods in various all-in-one IR settings while offering a scalable and generalizable solution for challenging unseen IR scenarios.

* indicates corresponding author: Hong Liu <hongliu@pku.edu.cn>.

1 INTRODUCTION

Image Restoration (IR) aims to recover clean images from inputs degraded by diverse real-world corruptions such as noise, blur, haze, rain, and low-light conditions (Zamir et al., 2022; Li et al., 2023a; Ren et al., 2024; Potlapalli et al., 2024). A central challenge is *degradation-agnostic restoration*: developing a single model that can generalize across heterogeneous degradations. Despite recent progress, existing approaches often face an efficiency–performance dilemma. On the one hand, heavyweight designs based on prompts, instructions, or large vision–language models provide versatility but incur substantial computational cost (Potlapalli et al., 2024; Zamfir et al., 2025; Jiang et al., 2025). On the other hand, lightweight solutions improve efficiency at the expense of restoration quality (Li et al., 2022; Tang et al., 2025b). Achieving both robustness and efficiency within a unified framework remains an open problem.

This difficulty can be better understood from two complementary perspectives. First, different degradation types impose fundamentally different representational requirements: additive corruptions (*e.g.*, noise, rain) primarily affect local textures, multiplicative distortions (*e.g.*, haze, low-light) require global context modeling, and kernel-based degradations (*e.g.*, blur) call for multi-scale structural reasoning. At the same time, basic architectural modules exhibit distinct inductive biases: convolutional filters excel at local texture modeling, attention mechanisms capture long-range dependencies, and MLPs enhance channel statistics. This motivates the insight that *an effective restoration model should systematically align distinct modules with complementary representational functions*. Second, recent studies reveal substantial redundancy in attention-based models, particularly along the channel dimension (Venkataramanan et al., 2024; Dong et al., 2021). Many channels encode overlapping information, suggesting that this redundancy could be *repurposed* rather than discarded. Leveraging this observation allows for architectures that remain compact while preserving expressive capacity. These observations highlight that unified IR benefits not only from adding new modules, but from a principled reorganization of existing capacity based on redundancy patterns and complementary inductive biases. This perspective motivates our design philosophy in MIRAGE, where representational roles are explicitly aligned with structural evidence rather than heuristic module stacking.

Building on these insights, we present MIRAGE, an efficient framework for degradation-agnostic image restoration. MIRAGE introduces two components. (i) *Channel-wise functional decomposition*, where the input feature map is partitioned along the channel dimension and processed by three specialized branches: convolution for local textures, attention for global context, and MLP for channel statistics. This structured decomposition repurposes redundant capacity into complementary roles, yielding both interpretability and strong efficiency–performance trade-offs. (ii) *Manifold regularization*, a cross-layer contrastive strategy that leverages natural feature pairs within the model. Inspired by deeply supervised networks (Lee et al., 2015), we hypothesize that natural contrastive pairs exist between shallow and latent representations. Shallow features preserve fine spatial details but are sensitive to noise, while latent features are more abstract and semantically stable; aligning them encourages more robust shared representations. Importantly, rather than computing contrastive loss in Euclidean space, which may distort similarity when comparing structured representations, we operate in the Symmetric Positive Definite (SPD) manifold space. This formulation provides a more faithful alignment of representations, leading to improved generalization across degradation types. Overall, MIRAGE provides a structurally grounded view of unified IR, where representational capacity is allocated and aligned based on statistical evidence at both the spatial and depth levels.

Extensive experiments across five degradation settings show that MIRAGE achieves state-of-the-art performance with remarkable efficiency: our model has only 6M parameters, more than five times smaller than recent prompt-based baselines, while also generalizing well to unseen scenarios such as underwater image enhancement. Both the visual and per-setting PSNR results are shown in Fig. 1.

Our contributions are summarized as follows:

- We propose a principled channel-wise functional decomposition strategy that aligns convolution, attention, and MLP with distinct representational roles, enabling efficient and effective degradation-agnostic restoration.
- We introduce manifold regularization through cross-layer contrastive alignment between shallow and latent features. We exploit natural contrastive pairs within the model, and per-

form this alignment in the SPD manifold space rather than Euclidean space, providing more faithful representation similarity and improved generalization across diverse degradations.

- We conduct comprehensive experiments across single, mixed, and unseen degradation settings, establishing MIRAGE as a strong and practical baseline for all-in-one IR.

2 RELATED WORK

Image Restoration with Various Architectures. IR addresses the ill-posed problem of retoring high-quality images from degraded inputs and has long been a core task in computer vision with broad applications (Richardson, 1972; Banham & Katsaggelos, 1997; Xie et al., 2025; Li et al., 2023b; Zamfir et al., 2024). Early methods relied on model-based formulations with handcrafted priors, but deep learning has shifted the field toward data-driven approaches, including regression-based (Lim et al., 2017; Lai et al., 2017; Liang et al., 2021; Chen et al., 2021; Li et al., 2023a; Zhang et al., 2024) and generative pipelines (Gao et al., 2023; Wang et al., 2023b; Luo et al., 2023; Yue et al., 2023; Zhao et al., 2024). These methods employ diverse backbones: convolutional networks for local structures (Dong et al., 2015; Zhang et al., 2017b;a; Wang et al., 2018), MLPs and state space models for channel or sequential dependencies (Tu et al., 2022; Guo et al., 2024a; Zhu et al., 2024; Gu & Dao, 2023; Dao & Gu, 2024; Tang et al., 2025a), and Transformers for long-range interactions (Liang et al., 2021; Ren et al., 2023; Li et al., 2023a; Zamir et al., 2022; Dosovitskiy et al., 2020; Liu et al., 2023; Shi et al., 2025), achieving promising results. Despite these advances, most IR solutions remain degradation-specific, addressing tasks such as denoising (Zhang et al., 2019), dehazing (Wu et al., 2021), deraining (Jiang et al., 2020), or deblurring (Kong et al., 2023), motivating the need for unified frameworks that generalize across diverse degradations while remaining efficient.

Degradation-agnostic Image Restoration. While training task-specific models for individual degradations can be effective, it is impractical to maintain separate models for each corruption. Real-world images often suffer from mixed degradations, making independent treatment infeasible, and task-specific approaches further increase computational and storage costs, amplifying their environmental footprint. To overcome these limitations, the emerging field of degradation-agnostic IR focuses on single-blind models capable of handling multiple degradation types simultaneously (Zamfir et al., 2025; Zeng et al., 2025; Zheng et al., 2024b; Ren et al., 2026). For example, AirNet (Li et al., 2022) achieves blind All-in-One image restoration by using contrastive learning to derive degradation representations from corrupted images, which are then leveraged to reconstruct clean images. Building on this, IDR (Zhang et al., 2023) tackles the problem by decomposing degradations into fundamental physical components and applying a two-stage meta-learning strategy. More recently, the extra learnable prompt-based paradigm (Potlapalli et al., 2024; Wang et al., 2023a; Li et al., 2023c; Tian et al., 2025) has introduced a visual prompt learning module, enabling a single model to better handle diverse degradation types by leveraging the discriminative capacity of learned visual prompts. Extending this idea, some works further model prompts from a frequency perspective (Cui et al., 2025) or propose more complex architectures with additional datasets (Dudhane et al., 2024). However, visual prompt modules often result in increased training time and decreased efficiency (Cui et al., 2025). Meanwhile, inspired by recent advances in self-supervised learning, several works (Wu et al., 2021; Chen et al., 2022c) have explored contrastive objectives to enhance low-level representations, though mainly within single-task IR scenarios. For the degradation-agnostic setting (Jiang et al., 2025; Li et al., 2022; Chen et al., 2025b; Zhang et al., 2025), the most recent DA-RCOT (Tang et al., 2025b) introduces a contrastive loss applied to residual feature space, illustrating that contrastive signals can also benefit unified IR models. In contrast, our work aims to improve the model’s ability to capture representative degradation cues within the SPD space without relying on heavy or complex prompt designs. Our goal in this work is to develop a degradation-agnostic image restorer that remains both computationally efficient and environmentally sustainable.

3 PRELIMINARY: DEGRADATION-AWARE ARCHITECTURES FOR IR

Image Degradation and Restoration. Image restoration seeks to recover a clean image \mathbf{x} from a degraded observation \mathbf{y} :

$$\mathbf{y} = \mathcal{D}(\mathbf{x}) + \mathbf{n}, \tag{1}$$

where $\mathcal{D}(\cdot)$ denotes a degradation operator and \mathbf{n} noise. Real-world degradations are diverse—additive (*e.g.*, Gaussian noise, rain: $\mathbf{y} = \mathbf{x} + \mathbf{n}$), multiplicative (*e.g.*, haze, speckle: $\mathbf{y} = \mathbf{x} \cdot \mathbf{m}$), or convolutional

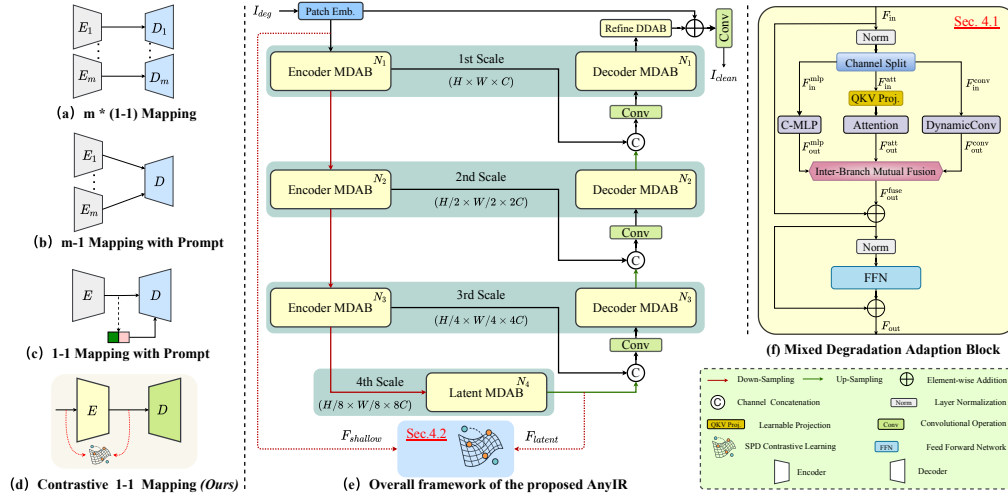


Figure 2: (a)-(c): The most adopted all-in-one image restoration encoder-decoder pipelines. (d): The toy illustration of our SPD contrastive pipeline. (e): The overall framework of the proposed MIRAGE : *i.e.*, a convolutional patch embedding, a U-shape encoder-decoder main body, an extra refined block, and the proposed SPD contrastive learning algorithm. (f): Structure of each mixed degradation adaptation block (MDAB).

(*e.g.*, blur, super-resolution: $\mathbf{y} = \mathbf{k} * \mathbf{x} + \mathbf{n}$) (He et al., 2025). These factors often co-occur and are spatially variant (Zhai et al., 2023), forming compound pipelines:

$$\mathbf{y} = \mathcal{D}_3(\mathcal{D}_2(\mathcal{D}_1(\mathbf{x}))) + \mathbf{n}. \quad (2)$$

Such complexity demands models that preserve local details while reasoning about global structures.

Architectural Biases for Degradation Modeling. Deep networks embody distinct inductive biases: *CNNs* capture local spatial patterns: $\mathbf{y}_p = \sum_i i \in \mathcal{N}(p) w_i \cdot \mathbf{x}_i$, effective for uniform or spatially invariant degradations. *Transformers* exploit global self-attention: $\mathbf{y}_i = \sum_j \alpha_{ij} \cdot \mathbf{V}_j$, well-suited for non-uniform, structured degradations (*e.g.* haze, patterned noise). *MLPs*, especially token-mixing forms, apply flexible position-wise mappings: $\mathbf{y} = \mathbf{W}_2 \cdot \phi(\mathbf{W}_1 \cdot \mathbf{x})$, though with weak spatial priors.

Each paradigm shows strengths yet clear limitations—*CNNs* excel in local fidelity, *Transformers* in global reasoning, and *MLPs* in flexible feature interactions, but lack inductive structure. Alone, they are insufficient for complex degradations and often parameter-heavy. Their complementarity motivates unified, degradation-aware architectures that leverage all three for robust IR in the wild.

4 THE PROPOSED MIRAGE

The design of MIRAGE is guided by two empirical observations. (i) Attention features consistently exhibit low-rank channel redundancy across scales (Fig. 3), indicating that a non-trivial portion of the representational capacity can be reassigned without loss of expressiveness. (ii) Different degradations favor complementary inductive biases, *i.e.*, local texture sensitivity, global contextual aggregation, and channel-statistical modulation. These observations motivate a principled partition of feature channels into convolutional, attention, and MLP pathways, allowing each subspace to specialize in the bias it is best suited for while maintaining overall model compactness. In parallel, the depth-asymmetric covariance structures of shallow and latent representations provide a natural basis for cross-layer alignment, for which the SPD formulation offers a geometry-preserving representation.

Prior works either train a separate model per degradation (Fig. 2a), adopt multi-encoder–single-decoder designs that inflate parameters (Fig. 2b), or rely on large-scale prompt-based models with visual/textual cues (Fig. 2c). In contrast, we propose a simple yet effective mixed-backbone architecture (Fig. 2d), which already forms a strong restoration baseline (Sec. 4.1) and is further enhanced by cross-layer contrastive learning in SPD space between shallow and latent features (Sec. 4.2).

4.1 MIXED DEGRADATION ADAPTATION BLOCK FOR DEGRADATION-AGNOSTIC IR

Algorithm 1 Mixed Parallel Degradation Adaptation

Require: $F_{in}^{att}, F_{in}^{conv}, F_{in}^{mlp}$	▷ Input features from three branches
Ensure: F_{out}	▷ Final fused output
[Att] Attention Path	
1: $Q, K, V \leftarrow \text{Linear}(F_{in}^{att})$	▷ Projection to attention tokens
2: $F_{out}^{att} \leftarrow \text{Softmax}(\frac{QK^T}{\sqrt{d}})V$	▷ Multi-head self-attention
[Conv] Dynamic Convolution Path	
3: $F' \leftarrow \text{Conv}1 \times 1(\text{Norm}(F_{in}^{conv}))$	▷ Normalization and expansion
4: $\gamma, \beta, \alpha \leftarrow \text{Split}(F')$	▷ Gating, intermediate, convolutional paths
5: $\alpha' \leftarrow \text{DynamicDepthwiseConv}(\alpha)$	▷ Content-adaptive depthwise conv
6: $\hat{F} \leftarrow \sigma(\gamma/\tau) \cdot \text{Concat}(\beta, \alpha')$	▷ Gated local enhancement
7: $F_{out}^{conv} \leftarrow \text{Conv}1 \times 1(\hat{F}) + F_{in}^{conv}$	▷ Residual projection
[MLP] MLP Path	
8: $F_{out}^{mlp} \leftarrow \text{MLP}(F_{in}^{mlp})$	▷ Channel-wise transformation brings more non-linearity
[Fusion] Inter-Branch Mutual Fusion	
9: $F_{out}^{att'} \leftarrow F_{out}^{att} + \lambda_{att} \cdot \sigma(F_{out}^{conv} + F_{out}^{mlp})$	▷ Fuse conv and MLP into attention
10: $F_{out}^{conv'} \leftarrow F_{out}^{conv} + \lambda_{conv} \cdot \sigma(F_{out}^{att} + F_{out}^{mlp})$	▷ Fuse attention and MLP into conv
11: $F_{out}^{mlp'} \leftarrow F_{out}^{mlp} + \lambda_{mlp} \cdot \sigma(F_{out}^{att} + F_{out}^{conv})$	▷ Fuse attention and conv into MLP
Output Projection	
12: $F_{out}^{fuse} \leftarrow \text{Project}(\text{Concat}(F_{out}^{att'}, F_{out}^{conv'}, F_{out}^{mlp'}))$	▷ Final unified representation
13: return F_{out}^{fuse}	

Redundancy in MHAs Opens Opportunities for Hybrid Architectures.

Redundancy has long been recognized as a fundamental limitation in multi-head self-attention (MHA), the core building block of Transformers, in both NLP and vision domains (Nguyen et al., 2022b;a; Xiao et al., 2024; Brödermann et al., 2025; Wang et al., 2022; Venkataraman et al., 2024). Prior studies indicated that not all attention heads contribute equally, *i.e.*, some are specialized and crucial, while others can be pruned with negligible impact. *This inherently implies redundancy in the channel dimension, as MHA outputs are concatenated along this axis.*

To empirically verify this redundancy in the context of IR, we analyze intermediate features from a lightweight attention-only model (details in the Appendix A). Specifically, we compute cumulative explained variance via PCA and normalized singular value spectra via SVD across multiple feature scales. Fig. 3(a) shows earlier scales (*e.g.*, 1st Scale) need far fewer principal components to retain most variance, suggesting high redundancy. Fig. 3(b) further supports this, with a sharper singular value decay at shallower stages, indicating stronger low-rank structure in channel-wise representations. Even at the deepest stage (*e.g.*, 4th Scale), achieving 90% variance requires only 31 of 192 components ($\approx 16\%$), confirming redundancy persists throughout.

This insight motivates a departure from traditional head/channel pruning. Instead of discarding redundant capacity, we propose to *repurpose* it by splitting the channel dimension into three parts and feeding them into distinct architectural branches, *i.e.*, attention, convolution, and MLP. This hybrid formulation leverages complementary inductive biases and makes full use of available representational space, offering a principled and efficient alternative to the previous pure MSA-based designs.

Parallel Design Brings More Efficiency. As shown in Lines 1–8 of Alg. 1, we instantiate this idea through a structurally parallel design that simultaneously exploits complementary inductive biases. As illustrated in Fig. 2(f), the input feature $F_{in} \in \mathbb{R}^{h \times w \times c}$ is evenly partitioned along the channel dimension into three sub-tensors (*i.e.*, F_{in}^{att} , F_{in}^{conv} , and F_{in}^{mlp}), which are then processed in parallel by

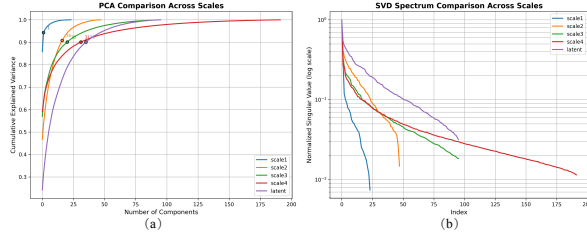


Figure 3: Channel redundancy analysis across multiple feature scales. (a) Cumulative explained variance curves from PCA applied to the channel dimension of features from 1-4 scales and one latent scale. (b) Normalized singular value spectra (in log scale) of the same features via SVD. Latent feature in both plots means the channel-wise projected 4th Scale feature.

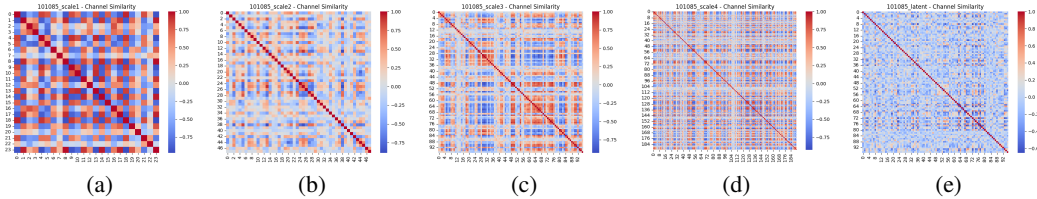


Figure 4: (a)-(d): The channel-wise similarity matrix from the 1st Scale ($H \times W \times C$) to the 4th Scale ($H/s \times W/s \times 8C$). (e): The channel-wise similarity matrix of (d) after channel-wise projection.

attention, convolution, and MLP branches. Each branch operates only on its allocated fraction of channels, substantially reducing computational cost, while its architectural heterogeneity enriches the representational space. This parallel decomposition achieves a favorable balance between efficiency and expressiveness, in contrast to prior designs that rely on purely attention-based processing.

Inter-Branch Mutual Fusion Injects Expressivity Before FFN. While the parallel design improves efficiency and modularity, it reduces interaction across branches. To mitigate this, Lines 9–13 of Alg. 1 introduce an inter-branch fusion mechanism, where each branch is enhanced via gated aggregation of the rest, modulated by learnable coefficients λ . This introduces cross-path context blending, reinforcing feature complementarity before unification, forming an effective pre-FFN encoder.

Compared to the attention-only models, the fused output in Alg. 1 introduces richer interactions. This enhances the model’s ability to fit complex degradation mappings, making it more suitable for mixed or ambiguous degradations. Subsequently, layer normalization, a feed-forward network (FFN), and a residual connection are applied: $F_{\text{out}} = \text{FFN}(\text{Norm}(F_{\text{out}}^{\text{fuse}})) + F_{\text{out}}^{\text{fuse}}$. This sequence stabilizes feature distributions and further boosts expressiveness.

4.2 SHALLOW-LATENT CONTRASTIVE LEARNING VIA SPD MANIFOLD ALIGNMENT

The unified IR model requires a single backbone to process degradations that depend on fundamentally different representational levels. Shallow layers primarily encode degradation-specific, fine-grained structures, whereas deeper layers become more semantic and statistically stable. This inherent depth asymmetry introduces representation drift when multiple degradations share the same feature space, motivating a mechanism that explicitly enforces cross-stage consistency. We therefore treat shallow and latent features as complementary views of the underlying signal and align them to stabilize the shared representation space, thereby improving generalization across heterogeneous degradations.

Shallow-Latent Feature Pairs are Naturally Contrastive Pairs. Features extracted at different depths exhibit fundamentally different statistical properties. As shown in Fig. 4, shallow-stage features (e.g., Scale1) present *sparse and decorrelated channel distributions*, while deeper layers (e.g., Scale4) become *increasingly redundant and concentrated*. This trend is quantitatively supported by the effective rank ratio across scales, which increases from only 4.2% ($1/24$ at 1st Scale) to 16.1% ($31/192$ at 4th Scale). However, by compressing the deep features through a lightweight MLP, we obtain a latent representation with a notably higher rank ratio of 36.5% ($35/96$), indicating a more decorrelated and expressive embedding. This structural disparity between sparse, localized shallow features and compressed, semantic latent ones naturally defines a contrastive pairing without requiring augmentation. We leverage this depth-asymmetric contrast to impose consistency across stages, enabling better semantic alignment and stronger representational generalization under complex degradation conditions. *Note that this study is conducted under noise degradation; however, similar trends are consistently observed for other degradations as well.* See the appendix for more details.

SPD Manifold Space Contrastive Learning Leads to More Discriminative Representations. To enhance representation consistency across depth, we introduce a contrastive objective defined over SPD (Symmetric Positive Definite) manifold features. We note that the goal here is not to perform full Riemannian optimization along SPD geodesics. Instead, we adopt a lightweight formulation that retains the key second-order structure of covariance matrices while keeping training stable and efficient. Strict geodesic contrastive learning typically requires repeated log/exp mappings and matrix decompositions, which incur considerable overhead in large low-level vision models. Our approach strikes a practical balance by preserving essential SPD structure before projection. Specifically, in our work, given shallow features $F_{\text{shallow}} \in \mathbb{R}^{C_s \times H \times W}$ and latent features $F_{\text{latent}} \in \mathbb{R}^{C_l \times H' \times W'}$, we first reduce their channel dimensions via 1×1 convolutions. The resulting tensors are reshaped into

feature matrices $X_s, X_l \in \mathbb{R}^{C \times N}$ with $N = H \times W$, and their second-order statistics are computed as:

$$\mathbf{C}_s = \frac{1}{N-1}(X_s - \mu_s)(X_s - \mu_s)^\top + \epsilon \mathbf{I}, \quad \mathbf{C}_l = \frac{1}{N'-1}(X_l - \mu_l)(X_l - \mu_l)^\top + \epsilon \mathbf{I}, \quad (3)$$

where μ is the mean across spatial dimensions, and $\epsilon \mathbf{I}$ ensures numerical stability and positive definiteness. The SPD matrices $\mathbf{C}_s, \mathbf{C}_l \in \mathbb{R}^{C \times C}$ are vectorized and projected to a contrastive embedding space via shallow 1-layer MLPs:

$$z_s = \text{Norm}(W_s \cdot \text{vec}(\mathbf{C}_s)), \quad z_l = \text{Norm}(W_l \cdot \text{vec}(\mathbf{C}_l)), \quad (4)$$

where W_s, W_l are learnable projection layers, and $\text{Norm}(\cdot)$ denotes ℓ_2 -normalization. We then apply an InfoNCE-style contrastive loss to align the shallow and latent embeddings:

$$\mathcal{L}_{\text{SPD}} = -\log \frac{\exp(\text{sim}(z_s, z_l)/\tau)}{\sum_{z'_l} \exp(\text{sim}(z_s, z'_l)/\tau)}, \quad (5)$$

where $\text{sim}(\cdot, \cdot)$ denotes cosine similarity and τ a temperature parameter. Unlike Euclidean contrastive learning, which views features as flat vectors, our SPD-based method preserves second-order channel dependencies, providing richer structural supervision. This regularization aligns local and semantic features across depth, enhances discriminability, and *introduces no additional inference cost*.

5 EXPERIMENTS

We conduct experiments adhering to the protocols of prior general image restoration works (Potlapalli et al., 2024; Zhang et al., 2023) under 5 settings: (a) 3 Degradations, (b) 5 Degradations, (c) Mixed Degradation, (d) Adverse Weather Removal, and (e) Zero-Shot. The implementation and experimental details, and the dataset description are provided in the appendix. Our code, checkpoints, and visual results are available via: <https://github.com/Amazingren/MIRAGE>.

5.1 SOTA COMPARISON.

3 Degradations. We evaluate our method against others listed in Tab. 1, all trained on three degradations: dehazing, deraining, and denoising. MIRAGE consistently outperforms all the comparison methods, even for those with the assistance of language, multi-task, or prompts. Notably, even our **6M** tiny model outperforms our baseline PromptIR by **0.71dB** on average. Our 10M small model achieves the best performance across all the metrics, with **60%** fewer parameters compared MoCE-IR. Compared to DA-RCOT (Tang et al., 2025b), which performs contrastive learning over residual feature space, MIRAGE achieves consistently better restoration quality while using substantially fewer parameters (10M vs. 50M). This highlights the efficiency and effectiveness of our SPD-based cross-layer alignment despite its more compact design.

5 Degradations. Extending the 3 tasks with deblurring and low-light enhancement (Li et al., 2022; Zhang et al., 2023), we evaluate our MIRAGE’s performance in a more challenging 5-degradation setting. Tab. 2 shows that MIRAGE -S surpasses PromptIR (Potlapalli et al., 2024), MoCE-IR-S (Zamfir et al., 2025), AdaIR (Cui et al., 2025), and VLU-Net (Zeng et al., 2025) by **1.53dB**, **0.6dB**, **0.48dB**, and **0.57dB** on average, with fewer parameters. Our tiny model (6M) also achieves a second-best average PSNR against MoCE-IR (25M) and surpasses all other methods, including those aided by additional modalities, multi-task learning, or pretraining.

Mixed Degradations. To better approximate real-world conditions, we extend OneRestore (Guo et al., 2024b) to cover both diverse single degradations (rain, haze, snow, low light) and composite cases with multiple degradations per image, yielding eleven distinct restoration settings. As shown in Tab. 3, MIRAGE consistently outperforms leading approaches including AirNet (Li et al., 2022), PromptIR (Potlapalli et al., 2024), WGWSNet (Zhu et al., 2023), WeatherDiff (Özdenizci & Legenstein, 2023), OneRestore (Guo et al., 2024b), and MoCE-IR (Zamfir et al., 2025). Specifically, our Tiny (6M) and Small (10M) models outperform OneRestore (Guo et al., 2024b) (6M) by **0.39 dB** and **0.86dB** on average. Compared to the recent SOTA MoCE-IR (Zamfir et al., 2025) (11M), our Small model achieves **0.28dB** higher performance with fewer parameters (10M vs. 11M). These results highlight the effectiveness of our method, particularly for complex mixed degradations.

Table 1: Comparison to state-of-the-art on three degradations. PSNR (dB, \uparrow) and SSIM (\uparrow) metrics are reported on the full RGB images. **Best** performances is highlighted. ‘-’ means unreported results.

Method	Venue.	Params.	Dehazing		Deraining		Denoising			Average				
			SOTS		Rain100L		BSD68 $_{\sigma=15}$	BSD68 $_{\sigma=25}$	BSD68 $_{\sigma=50}$					
BRDNet (Tian et al., 2020)	NN’20	-	23.23	.895	27.42	.895	32.26	.898	29.76	.836	26.34	.693	27.80	.843
LPNet (Gao et al., 2019)	CVPR’19	-	20.84	.828	24.88	.784	26.47	.778	24.77	.748	21.26	.552	23.64	.738
FDGAN (Dong et al., 2020)	AAAI’20	-	24.71	.929	29.89	.933	30.25	.910	28.81	.868	26.43	.776	28.02	.883
DL (Fan et al., 2019)	TPAMI’19	2M	26.92	.931	32.62	.931	33.05	.914	30.41	.861	26.90	.740	29.98	.876
MPRNet (Zamfir et al., 2021)	CVPR’21	16M	25.28	.955	33.57	.954	33.54	.927	30.89	.880	27.56	.779	30.17	.899
AirNet (Li et al., 2022)	CVPR’22	9M	27.94	.962	34.90	.967	33.92	.933	31.26	.888	28.00	.797	31.20	.910
NDR (Yao et al., 2024)	TIP’24	28M	25.01	.860	28.62	.848	28.72	.826	27.88	.798	26.18	.720	25.01	.810
PromptIR (Potlapalli et al., 2024)	NeurIPS’23	36M	30.58	.974	36.37	.972	33.98	.933	31.31	.888	28.06	.799	32.06	.913
MoCE-IR-S (Zamfir et al., 2025)	CVPR’25	11M	30.98	.979	38.22	.983	34.08	.933	31.42	.888	28.16	.798	32.57	.916
AdaIR (Cui et al., 2025)	ICLR’25	29M	31.06	.980	38.64	.983	34.12	.935	31.45	.892	28.19	.802	32.69	.918
MoCE-IR (Zamfir et al., 2025)	CVPR’25	25M	31.34	.979	38.57	.984	34.11	.932	31.45	.888	28.18	.800	32.73	.917
DA-RCOT (Tang et al., 2025b)	TPAMI’25	50M	31.26	.977	38.36	.983	33.98	.934	31.33	.890	28.10	.801	32.60	.917
MIRAGE -T (Ours)	ICLR’26	6M	31.81	.982	38.44	.983	34.05	.935	31.40	.892	28.14	.802	32.77	.919
MIRAGE -S (Ours)	ICLR’26	10M	31.86	.981	38.94	.985	34.12	.935	31.46	.891	28.19	.803	32.91	.919
Methods with the assistance of vision language, multi-task learning, natural language prompts, or multi-modal control														
DA-CLIP (Luo et al., 2024)	ICLR’24	125M	29.46	.963	36.28	.968	30.02	.821	24.86	.585	22.29	.476	-	-
Art _{PromptIR} (Wu et al., 2024)	ACM MM’24	36M	30.83	.979	37.94	.982	34.06	.934	31.42	.891	28.14	.801	32.49	.917
InstructIR-3D (Conde et al., 2024)	ECCV’24	16M	30.22	.959	37.98	.978	34.15	.933	31.52	.890	28.30	.804	32.43	.913
UniProcessor (Duan et al., 2025)	ECCV’24	1002M	31.66	.979	38.17	.982	34.08	.935	31.42	.891	28.17	.803	32.70	.918
VLU-Net (Zeng et al., 2025)	CVPR’25	35M	30.71	.980	38.93	.984	34.13	.935	31.48	.892	28.23	.804	32.70	.919
RamIR (Tang et al., 2025a)	Applied’25	21.7M	31.29	.977	38.16	.981	34.04	.931	31.61	.891	28.19	.801	32.65	.916

Table 2: Comparison to state-of-the-art on five degradations. PSNR (dB, \uparrow) and SSIM (\uparrow) metrics are reported on the full RGB images with (*) denoting general image restorers, others are specialized all-in-one approaches. **Best** performance is highlighted.

Method	Venue	Params.	Dehazing		Deraining		Denoising		Deblurring		Low-Light		Average	
			SOTS		Rain100L		BSD68 $_{\sigma=25}$		GoPro		LOLv1			
NAFNet* (Chen et al., 2022a)	ECCV’22	17M	25.23	.939	35.56	.967	31.02	.883	26.53	.808	20.49	.809	27.76	.881
DGUNet* (Mou et al., 2022)	CVPR’22	17M	24.78	.940	36.62	.971	31.10	.883	27.25	.837	21.87	.823	28.32	.891
SwinIR* (Liang et al., 2021)	ICCVW’21	1M	21.50	.891	30.78	.923	30.59	.868	24.52	.773	17.81	.723	25.04	.835
Restormer* (Zamfir et al., 2022)	CVPR’22	26M	24.09	.927	34.81	.962	31.49	.884	27.22	.829	20.41	.806	27.60	.881
MambaIR* (Guo et al., 2024a)	ECCV’24	27M	25.81	.944	36.55	.971	31.41	.884	28.61	.875	22.49	.832	28.97	.901
DL (Fan et al., 2019)	TPAMI’19	2M	20.54	.826	21.96	.762	23.09	.745	19.86	.672	19.83	.712	21.05	.743
Transweather	CVPR’22	38M	21.32	.885	29.43	.905	29.00	.841	25.12	.757	21.21	.792	25.22	.836
TAPE (Liu et al., 2022)	ECCV’22	1M	22.16	.861	29.67	.904	30.18	.855	24.47	.763	18.97	.621	25.09	.801
AirNet (Li et al., 2022)	CVPR’22	9M	21.04	.884	32.98	.951	30.91	.882	24.35	.781	18.18	.735	25.49	.847
IDR (Zhang et al., 2023)	CVPR’23	15M	25.24	.943	35.63	.965	31.60	.887	27.87	.846	21.34	.826	28.34	.893
PromptIR (Potlapalli et al., 2024)	NeurIPS’23	36M	30.41	.972	36.17	.970	31.20	.885	27.93	.851	22.89	.829	29.72	.901
MoCE-IR-S (Zamfir et al., 2025)	CVPR’25	11M	31.33	.978	37.21	.978	31.25	.884	28.90	.877	21.68	.851	30.08	.913
AdaIR (Cui et al., 2025)	ICLR’25	29	30.53	.978	38.02	.981	31.35	.889	28.12	.858	23.00	.845	30.20	.910
MoCE-IR (Zamfir et al., 2025)	CVPR’25	25M	30.48	.974	38.04	.982	31.34	.887	30.05	.899	23.00	.852	30.58	.919
DA-RCOT (Tang et al., 2025b)	TPAMI’25	50M	30.96	.975	37.87	.980	31.23	.888	28.68	.872	23.25	.836	30.40	.911
MIRAGE -T (Ours)	ICLR’26	6M	31.35	.979	38.24	.983	31.35	.891	27.98	.850	23.11	.854	30.41	.912
MIRAGE -S (Ours)	ICLR’26	10M	31.45	.980	38.92	.985	31.41	.892	28.10	.858	23.59	.858	30.68	.914
Methods with the assistance of natural language prompts or multi-task learning														
InstructIR-5D (Conde et al., 2024)	ECCV’24	16M	36.84	.973	27.10	.956	31.40	.887	29.40	.886	23.00	.836	29.55	.908
Art _{PromptIR} (Wu et al., 2024)	ACM MM’24	36M	29.93	.908	22.09	.891	29.43	.843	25.61	.776	21.99	.811	25.81	.846
VLU-Net (Zeng et al., 2025)	CVPR’25	35M	30.84	.980	38.54	.982	31.43	.891	27.46	.840	22.29	.833	30.11	.905
RamIR (Tang et al., 2025a)	Applied’25	21.7M	31.09	.978	37.56	.979	31.44	.886	28.82	.878	22.02	.828	30.18	.910

Adverse Weather Removal. Following (Valanarasu et al., 2022; Zhu et al., 2023), We test our MIRAGE on three challenging deweathering tasks: snow removal, rain streak and fog removal, and raindrop removal. Tab. 4 shows the comparison of our MIRAGE and other state-of-the-art methods. MIRAGE consistently outperforms existing methods across almost all datasets except PSNR for RainDrop. The performance gains over multiple weather degradations demonstrate the effectiveness of MIRAGE in handling diverse weather conditions. Especially, **0.30dB** improvement on PSNR over Histoformer (Sun et al., 2024) and **1.05dB** improvements over MPerceiver (Ai et al., 2024).

Zero-Shot Setting. We evaluate our method’s generalization under a challenging zero-shot setting with real-world underwater images. As shown in Tab. 5, MIRAGE -S achieves 17.29 dB and 0.773 SSIM, surpassing MoCE-IR (Zamfir et al., 2025) by **+1.38dB** PSNR, while being more compact.

Table 3: Comparison to state-of-the-art on composited degradations. PSNR (dB, \uparrow) and SSIM (\uparrow) are reported on the full RGB images. Our method consistently outperforms even larger models, with favorable results in composited degradation scenarios.

Method	Params.	CDD11-Single				CDD11-Double					CDD11-Triple		Avg.												
		Low (L)	Haze (H)	Rain (R)	Snow (S)	L+H	L+R	L+S	H+R	H+S	L+H+R	L+H+S													
AirNet	9M	24.83	.778	24.21	.951	26.55	.891	26.79	.919	23.23	.779	22.82	.710	23.29	.723	22.21	.868	23.29	.901	21.80	.708	22.24	.725	23.75	.814
PromptIR	36M	26.32	.805	26.10	.969	31.56	.946	31.53	.960	24.49	.789	25.05	.771	24.51	.761	24.54	.924	23.70	.925	23.74	.752	23.33	.747	25.90	.850
WGWSNet	26M	24.39	.774	27.90	.982	33.15	.964	34.43	.973	24.27	.800	25.06	.772	24.60	.765	27.23	.955	27.65	.960	23.90	.772	23.97	.771	26.96	.863
WeatherDiff	83M	23.58	.763	21.99	.904	24.85	.885	24.80	.888	21.83	.756	22.69	.730	22.12	.707	21.25	.868	21.99	.868	21.23	.716	21.04	.698	22.49	.799
OneRestore	6M	26.48	.826	32.52	.990	33.40	.964	34.31	.973	25.79	.822	25.58	.799	25.19	.789	29.99	.957	30.21	.964	24.78	.788	24.90	.791	28.47	.878
MoCE-IR	11M	27.26	.824	32.66	.990	34.31	.970	35.91	.980	26.24	.817	26.25	.800	26.04	.793	29.93	.964	30.19	.970	25.41	.789	25.39	.790	29.05	.881
MIRAGE (ours)	6M	27.13	.830	32.39	.989	34.23	.969	35.57	.978	26.04	.823	26.21	.807	26.07	.799	29.49	.962	29.72	.967	25.17	.793	25.41	.793	28.86	.883
MIRAGE (ours)	10M	27.41	.833	33.12	.992	34.66	.971	35.98	.981	26.55	.828	26.53	.810	26.33	.803	30.32	.965	30.27	.969	25.59	.801	25.86	.799	29.33	.887

Table 4: Comparisons for 4-task adverse weather removal. Missing values are denoted by ‘-’.

Method	Venue	Snow100K-S		Snow100K-L		Outdoor-Rain		RainDrop		Average	
		PSNR	SSIM								
All-in-One (Li et al., 2020)	CVPR’20	-	-	28.33	.882	24.71	.898	31.12	.927	28.05	.902
TransWeather (Valanarasu et al., 2022)	CVPR’22	32.51	.934	29.31	.888	28.83	.900	30.17	.916	30.20	.909
Chen et al. (Chen et al., 2022b)	CVPR’22	34.42	.947	30.22	.907	29.27	.915	31.81	.931	31.43	.925
WGWSNet (Zhu et al., 2023)	CVPR’23	34.31	.946	30.16	.901	29.32	.921	32.38	.938	31.54	.926
WeatherDiff ₆₄ (Özdenizci & Legenstein, 2023)	TPAMI’23	35.83	.957	30.09	.904	29.64	.931	30.71	.931	31.57	.931
WeatherDiff ₁₂₈ (Özdenizci & Legenstein, 2023)	TPAMI’23	35.02	.952	29.58	.894	29.72	.922	29.66	.923	31.00	.923
AWRCP (Ye et al., 2023)	ICCV’23	36.92	.965	31.92	.934	31.39	.933	31.93	.931	33.04	.941
GridFormer (Wang et al., 2024)	IJCV’24	37.46	.964	31.71	.923	31.87	.933	32.39	.936	33.36	.939
MPerceiver (Ai et al., 2024)	CVPR’24	36.23	.957	31.02	.916	31.25	.925	33.21	.929	32.93	.932
DTPM (Ye et al., 2024)	CVPR’24	37.01	.966	30.92	.917	30.99	.934	32.72	.944	32.91	.940
Histoformer (Sun et al., 2024)	ECCV’24	37.41	.966	32.16	.926	32.08	.939	33.06	.944	33.68	.944
MIRAGE -S (Ours)	ICLR’26	37.97	.973	32.33	.929	32.82	.949	32.78	.945	33.98	.949

Table 5: Zero-Shot Cross-Domain Underwater Image Enhancement Results.

Method	PSNR (\uparrow)	SSIM (\uparrow)
SwinIR (Liang et al., 2021)	15.31	.740
NAFNet (Chu et al., 2022)	15.42	.744
Restormer (Zamir et al., 2022)	15.46	.745
AirNet (Li et al., 2022)	15.46	.745
IDR (Zhang et al., 2023)	15.58	.762
PromptIR (Potlapalli et al., 2024)	15.48	.748
MoCE-IR (Zamfir et al., 2025)	15.91	.765
MIRAGE -S (Ours)	17.29	.773

Table 6: Complexity Analysis. FLOPs are computed on an image of size 224×224 using a NVIDIA Tesla A100 (40G) GPU.

Method	PSNR (\uparrow)	Memory (\downarrow)	Params. (\downarrow)	FLOPs (\downarrow)
AirNet (Li et al., 2022)	31.20	4829M	8.93M	238G
PromptIR (Potlapalli et al., 2024)	32.06	9830M	35.59M	132G
IDR (Zhang et al., 2023)	-	4905M	15.34M	98G
AdaIR (Cui et al., 2025)	-	9740M	28.79M	124G
MoCE-IR-S (Zamfir et al., 2025)	32.51	4263M	11.48M	37G
MoCE-IR (Zamfir et al., 2025)	32.73	6654M	25.35M	75G
MIRAGE -T (Ours)	32.77	3729M	6.21M	16G
MIRAGE -S (Ours)	32.91	4810M	9.68M	27G

Importantly, our model never sees underwater data during training, yet our adaptive modeling not only fits mixed degradations but also transfers robustly to unseen conditions. Besides, we also followed the same experimental setting introduced by UniRestore Chen et al. (2025a) for the generalization ability evaluation. Meanwhile, the real-world evaluation presented in Tab. D shows that MIRAGE generalizes reliably to real-world, camera-captured degradations.

Efficiency Comparison. Tab. 6 compares PSNR, memory, parameters, and FLOPs. Our Tiny model (MIRAGE -T), with only 6.21M parameters and 16G FLOPs, delivers the best efficiency–performance trade-off, outperforming all prior methods, including larger models like PromptIR (Potlapalli et al., 2024) and MoCE-IR-S (Zamfir et al., 2025). It surpasses MoCE-IR-S by **+0.26 dB** while using less than half the computation, and even our Small variant (MIRAGE -S) exceeds full MoCE-IR in both PSNR (**+0.18dB**) and FLOPs (27G vs. 75G). These results confirm that our design achieves strong restoration quality without compromising efficiency.

Visual Comparison. MIRAGE effectively restores fine structural details and reliably suppresses subtle visual artifacts across diverse and unseen degradations (Fig. 1 and appendix).

5.2 ABLATION ANALYSIS & DISCUSSION

Components ablation. Tab. 7 shows starting from an attention-only setting (32.23 dB, 19.89M), we progressively integrate each module while reducing complexity.

Removing the dynamic convolution branch (*w/o DynamicConv*) causes a 0.56 dB drop, indicating its importance for local spatial modeling. The channel-wise MLP (*w/o C-MLP*) also plays a critical role, with a 0.38 dB performance loss. Naive concatenation (*w/o Fusion*) leads to a further 0.20 dB drop, confirming that explicit feature integration is more effective. On the regularization side, removing contrastive learning (*w/o CL & SPD*) or replacing SPD with Euclidean alignment degrades performance by 0.14 dB and 0.24 dB, indicating that structure-agnostic contrastive learning can misguide optimization, while manifold-aware alignment provides consistent benefits. Overall, each component contributes to the final performance. Our full model offers the best balance between accuracy and efficiency with only 6.21M parameters and 32.77 dB PSNR.

Why shallow-latent Contrastive Alignment Matters.

Different degradations rely on different feature levels: denoising and deraining benefit from shallow, texture-rich features, while dehazing and low-light enhancement require deeper semantic features; deblurring needs both. This heterogeneity makes unified modeling challenging. We therefore introduce contrastive alignment between shallow and latent stages to encourage semantic coordination. When shallow features dominate (*e.g.*, denoising), alignment guides latent features to be more task-relevant; when latent features dominate (*e.g.*, dehazing), shallow features inherit semantic consistency (Bertasius et al., 2015). Fig. 5 validates that contrastive alignment improves shallow-latent correlation, validating its necessity for cross-degradation generalization.

Why Euclidean Fails and Why SPD Works? (Deraining Case Study) Euclidean contrastive learning collapses shallow-latent alignment by enforcing indiscriminate similarity, reducing both diagonal and off-diagonal terms to trivial constants, and erasing task cues. SPD, by aligning covariance matrices on a Riemannian manifold, preserves second-order dependencies and guides updates along meaningful directions. In the deraining case (Figure 6), Euclidean CL degenerates into near-constant similarity (off-diag 0.00237, ratio 0.99), while SPD maintains diagonal dominance and non-trivial off-diagonal structure (0.0787, ratio 0.149), producing coherent patterns.

6 CONCLUSION

We presented MIRAGE, an efficient framework for degradation-agnostic image restoration that achieves a favorable balance between robustness and efficiency. Through channel-wise functional decomposition, the model repurposes redundant capacity into convolution-, attention-, and MLP-based branches, enabling complementary modeling of local textures, global context, and channel-wise statistics. To further enhance cross-degradation generalization, we introduced manifold regularization, aligning shallow and latent features in the SPD manifold space for more consistent and discriminative representations. Extensive experiments across diverse degradations, including mixed and unseen scenarios, demonstrate that MIRAGE achieves state-of-the-art performance. Inspired by the metaphor of a mirage, *i.e.*, revealing the hidden reality beneath visual distortions, our framework learns degradation-agnostic representations by balancing global, local, and channel-wise information, providing a scalable foundation for future research in degradation-agnostic IR.

Table 7: Ablation Study of MIRAGE -T under the 3-Degradation Setting with Tiny model.

Ablation	Params.	Results	
		PSNR (dB, \uparrow)	SSIM (\downarrow)
att-only (<i>Ours</i>)	19.89 M	32.23 (-0.54)	.912
<i>w/o</i> DynamicConv	9.43 M	32.21 (-0.56)	.911
<i>w/o</i> C-MLP	7.01 M	32.39 (-0.38)	.913
<i>w/o</i> Fusion (<i>i.e.</i> Cat()-Only)	5.71 M	32.57 (-0.20)	.914
<i>w/o</i> CL & SPD	5.80M	32.63 (-0.14)	.916
<i>w/o</i> SPD (CL Euclidean)	6.10M	32.53 (-0.24)	.914
MIRAGE -T (<i>Full</i>)	6.21M	32.77	.919

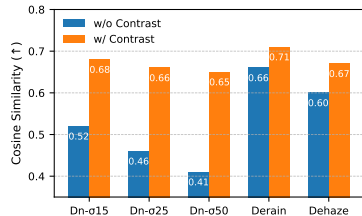


Figure 5: Shallow-latent cosine similarity across degradations. Contrastive alignment improves feature correlation.

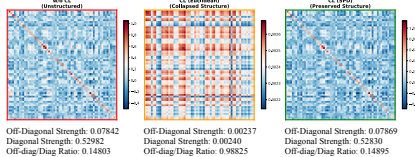


Figure 6: Shallow-latent similarity under three settings: (a) *w/o* CL (unstructured; off-diag 0.0784, ratio 0.148), (b) Euclidean CL (collapsed; off-diag \approx 0.0024, ratio 0.99), (c) SPD CL (preserved; off-diag 0.0787, ratio 0.149).

ACKNOWLEDGMENTS

This work was partially supported by the FIS project GUIDANCE (Debugging Computer Vision Models via Controlled Cross-modal Generation) (No. FIS2023-03251).

ETHICS STATEMENT

Our work focuses on general-purpose image restoration, aiming to improve efficiency and robustness across diverse degradation types. The intended positive impact includes deployment in low-resource or safety-critical scenarios such as mobile photography, remote sensing, medical imaging, and environmental monitoring. At the same time, we recognize that improved restoration techniques could be misused for deceptive content editing or large-scale surveillance. We encourage responsible use of our method and provide our models and code with appropriate licenses and documentation to support transparency and ethical adoption. No personally identifiable or sensitive data were used in this research.

REPRODUCIBILITY STATEMENT

We aim to ensure reproducibility and transparency of our results. The MIRAGE framework is implemented in PyTorch with standard training protocols and evaluation metrics. Detailed descriptions of the architecture, training settings, datasets, and baselines are provided in the main paper and supplementary material. Upon acceptance, we will release the full code, pretrained models, and instructions for reproducing all reported results, including ablation studies and comparisons. Random seeds and hardware details are also documented to facilitate faithful replication.

REFERENCES

- Yuang Ai, Huaibo Huang, Xiaoqiang Zhou, Jiexiang Wang, and Ran He. Multimodal prompt perceiver: Empower adaptiveness, generalizability and fidelity for all-in-one image restoration. In *CVPR*, pp. 25432–25444, 2024. 8, 9
- Pablo Arbelaez, Michael Maire, Charless Fowlkes, and Jitendra Malik. Contour detection and hierarchical image segmentation. *IEEE TPAMI*, 33(5):898–916, 2010. 1
- Mark R Banham and Aggelos K Katsaggelos. Digital image restoration. *IEEE Signal Processing Magazine*, 14(2):24–41, 1997. 3
- Gedas Bertasius, Jianbo Shi, and Lorenzo Torresani. High-for-low and low-for-high: Efficient boundary detection from deep object features and its applications to high-level vision. In *ICCV*, pp. 504–512, 2015. 10
- Tim Brödermann, Christos Sakaridis, Yuqian Fu, and Luc Van Gool. Cafuser: Condition-aware multimodal fusion for robust semantic perception of driving scenes. *RAL*, 2025. 5
- Bolun Cai, Xiangmin Xu, Kui Jia, Chunmei Qing, and Dacheng Tao. Dehazenet: An end-to-end system for single image haze removal. *IEEE TIP*, 25(11):5187–5198, 2016. 3
- I Chen, Wei-Ting Chen, Yu-Wei Liu, Yuan-Chun Chiang, Sy-Yen Kuo, Ming-Hsuan Yang, et al. Unirestore: Unified perceptual and task-oriented image restoration model using diffusion prior. In *CVPR*, pp. 17969–17979, 2025a. 9
- Lei Chen, Qingbo Xiong, Wei Zhang, Xiaoli Liang, Zhihua Gan, Liqiang Li, and Xin He. Multi-modal degradation feature learning for unified image restoration based on contrastive learning. *Neurocomputing*, 616:128955, 2025b. 3
- Liangyu Chen, Xiaojie Chu, Xiangyu Zhang, and Jian Sun. Simple baselines for image restoration. In *ECCV*, pp. 17–33, 2022a. 8
- Wei-Ting Chen, Zhi-Kai Huang, Cheng-Che Tsai, Hao-Hsiang Yang, Jian-Jiun Ding, and Sy-Yen Kuo. Learning multiple adverse weather removal via two-stage knowledge learning and multi-contrastive regularization: Toward a unified model. In *CVPR*, pp. 17632–17641, 2022b. 9

- Xiang Chen, Jinshan Pan, Kui Jiang, Yufeng Li, Yufeng Huang, Caihua Kong, Longgang Dai, and Zhentao Fan. Unpaired deep image deraining using dual contrastive learning. In *CVPR*, pp. 2017–2026, 2022c. 3
- Yinbo Chen, Sifei Liu, and Xiaolong Wang. Learning continuous image representation with local implicit image function. In *CVPR*, pp. 8628–8638, 2021. 3
- Xiaojie Chu, Liangyu Chen, and Wenqing Yu. Nafssr: Stereo image super-resolution using nafnet. In *CVPRWorkshops*, pp. 1239–1248, June 2022. 9
- Marcos V Conde, Gregor Geigle, and Radu Timofte. Instructir: High-quality image restoration following human instructions. In *ECCV*, 2024. 8
- Yuning Cui, Syed Waqas Zamir, Salman Khan, Alois Knoll, Mubarak Shah, and Fahad Shahbaz Khan. AdaIR: Adaptive all-in-one image restoration via frequency mining and modulation. In *ICLR*, 2025. 3, 7, 8, 9, 2, 10
- Tri Dao and Albert Gu. Transformers are SSMs: Generalized models and efficient algorithms through structured state space duality. In *ICML*, 2024. 3
- Chao Dong, Yubin Deng, Chen Change Loy, and Xiaoou Tang. Compression artifacts reduction by a deep convolutional network. In *ICCV*, pp. 576–584, 2015. 3
- Yihe Dong, Jean-Baptiste Cordonnier, and Andreas Loukas. Attention is not all you need: Pure attention loses rank doubly exponentially with depth. In *ICML*, pp. 2793–2803. PMLR, 2021. 2
- Yu Dong, Yihao Liu, He Zhang, Shifeng Chen, and Yu Qiao. Fd-gan: Generative adversarial networks with fusion-discriminator for single image dehazing. In *AAAI*, 2020. 8, 3
- Alexey Dosovitskiy, Lucas Beyer, Alexander Kolesnikov, Dirk Weissenborn, Xiaohua Zhai, Thomas Unterthiner, Mostafa Dehghani, Matthias Minderer, Georg Heigold, Sylvain Gelly, et al. An image is worth 16x16 words: Transformers for image recognition at scale. In *ICLR*, 2020. 3
- Huiyu Duan, Xiongkuo Min, Sijing Wu, Wei Shen, and Guangtao Zhai. Uniprocessor: a text-induced unified low-level image processor. In *ECCV*, pp. 180–199. Springer, 2025. 8
- Akshay Dudhane, Omkar Thawakar, Syed Waqas Zamir, Salman Khan, Fahad Shahbaz Khan, and Ming-Hsuan Yang. Dynamic pre-training: Towards efficient and scalable all-in-one image restoration. *arXiv preprint arXiv:2404.02154*, 2024. 3
- Qingnan Fan, Dongdong Chen, Lu Yuan, Gang Hua, Nenghai Yu, and Baoquan Chen. A general decoupled learning framework for parameterized image operators. *TPAMI*, 43(1):33–47, 2019. 8
- Hongyun Gao, Xin Tao, Xiaoyong Shen, and Jiaya Jia. Dynamic scene deblurring with parameter selective sharing and nested skip connections. In *CVPR*, 2019. 8, 4
- Sicheng Gao, Xuhui Liu, Bohan Zeng, Sheng Xu, Yanjing Li, Xiaoyan Luo, Jianzhuang Liu, Xiantong Zhen, and Baochang Zhang. Implicit diffusion models for continuous super-resolution. In *CVPR*, pp. 10021–10030, 2023. 3
- Albert Gu and Tri Dao. Mamba: Linear-time sequence modeling with selective state spaces. *arXiv preprint arXiv:2312.00752*, 2023. 3
- Hang Guo, Jinmin Li, Tao Dai, Zhihao Ouyang, Xudong Ren, and Shu-Tao Xia. Mambair: A simple baseline for image restoration with state-space model. In *ECCV*, 2024a. 3, 8
- Yu Guo, Yuan Gao, Yuxu Lu, Ryan Wen Liu, and Shengfeng He. Onerestore: A universal restoration framework for composite degradation. In *ECCV*, 2024b. 7, 1
- Chunming He, Yuqi Shen, Chengyu Fang, Fengyang Xiao, Longxiang Tang, Yulun Zhang, Wangmeng Zuo, Zhenhua Guo, and Xiu Li. Diffusion models in low-level vision: A survey. *TPAMI*, 2025. 4
- Jia-Bin Huang, Abhishek Singh, and Narendra Ahuja. Single image super-resolution from transformed self-exemplars. In *CVPR*, pp. 5197–5206, 2015. 1

- Hu JiaKui, Zhengjian Yao, Jin Lujia, and Lu Yanye. Universal image restoration pre-training via degradation classification. In *ICLR*, 2025. 2
- Junjun Jiang, Zengyuan Zuo, Gang Wu, Kui Jiang, and Xianming Liu. A survey on all-in-one image restoration: Taxonomy, evaluation and future trends. *IEEE TPAMI*, 2025. 2, 3
- Kui Jiang, Zhongyuan Wang, Peng Yi, Chen Chen, Baojin Huang, Yimin Luo, Jiayi Ma, and Junjun Jiang. Multi-scale progressive fusion network for single image deraining. In *CVPR*, pp. 8346–8355, 2020. 3, 4
- Diederik P Kingma and Jimmy Ba. Adam: A method for stochastic optimization. In *ICLR*, 2015. 2
- Lingshun Kong, Jiangxin Dong, Jianjun Ge, Mingqiang Li, and Jinshan Pan. Efficient frequency domain-based transformers for high-quality image deblurring. In *CVPR*, pp. 5886–5895, 2023. 3
- Wei-Sheng Lai, Jia-Bin Huang, Narendra Ahuja, and Ming-Hsuan Yang. Deep laplacian pyramid networks for fast and accurate super-resolution. In *CVPR*, pp. 624–632, 2017. 3
- Chen-Yu Lee, Saining Xie, Patrick Gallagher, Zhengyou Zhang, and Zhuowen Tu. Deeply-supervised nets. In *Artificial intelligence and statistics*, pp. 562–570. Pmlr, 2015. 2
- Boyi Li, Xiulian Peng, Zhangyang Wang, Jizheng Xu, and Dan Feng. Aod-net: All-in-one dehazing network. In *ICCV*, pp. 4770–4778, 2017. 3
- Boyi Li, Wenqi Ren, Dengpan Fu, Dacheng Tao, Dan Feng, Wenjun Zeng, and Zhangyang Wang. Benchmarking single-image dehazing and beyond. *TIP*, 28(1):492–505, 2018. 1
- Boyun Li, Xiao Liu, Peng Hu, Zhongqin Wu, Jiancheng Lv, and Xi Peng. All-in-one image restoration for unknown corruption. In *CVPR*, pp. 17452–17462, 2022. 2, 3, 7, 8, 9, 1, 4
- Chongyi Li, Chunle Guo, Wenqi Ren, Runmin Cong, Junhui Hou, Sam Kwong, and Dacheng Tao. An underwater image enhancement benchmark dataset and beyond. *TIP*, 29:4376–4389, 2019a. 2
- Ruoteng Li, Loong-Fah Cheong, and Robby T Tan. Heavy rain image restoration: Integrating physics model and conditional adversarial learning. In *CVPR*, pp. 1633–1642, 2019b. 1
- Ruoteng Li, Robby T Tan, and Loong-Fah Cheong. All in one bad weather removal using architectural search. In *CVPR*, pp. 3175–3185, 2020. 9
- Yawei Li, Yuchen Fan, Xiaoyu Xiang, Denis Demandolx, Rakesh Ranjan, Radu Timofte, and Luc Van Gool. Efficient and explicit modelling of image hierarchies for image restoration. In *CVPR*, pp. 18278–18289, 2023a. 2, 3
- Yawei Li, Kai Zhang, Jingyun Liang, Jiezhong Cao, Ce Liu, Rui Gong, Yulun Zhang, Hao Tang, Yun Liu, Denis Demandolx, Rakesh Ranjan, Radu Timofte, and Luc Van Gool. LSDIR: A large scale dataset for image restoration. In *CVPRW*, pp. 1775–1787, 2023b. 3
- Yawei Li, Bin Ren, Jingyun Liang, Rakesh Ranjan, Mengyuan Liu, Nicu Sebe, Ming-Hsuan Yang, and Luca Benini. Fractal-ir: A unified framework for efficient and scalable image restoration. *arXiv preprint arXiv:2503.17825*, 2025. 2
- Zilong Li, Yiming Lei, Chenglong Ma, Junping Zhang, and Hongming Shan. Prompt-in-prompt learning for universal image restoration. *arXiv preprint arXiv:2312.05038*, 2023c. 3
- Jingyun Liang, Jiezhong Cao, Guolei Sun, Kai Zhang, Luc Van Gool, and Radu Timofte. SwinIR: Image restoration using Swin transformer. In *ICCVW*, pp. 1833–1844, 2021. 3, 8, 9
- Bee Lim, Sanghyun Son, Heewon Kim, Seungjun Nah, and Kyoung Mu Lee. Enhanced deep residual networks for single image super-resolution. In *CVPRW*, pp. 1132–1140, 2017. 3
- Chang Liu, Mengyi Zhao, Bin Ren, Mengyuan Liu, Nicu Sebe, et al. Spatio-temporal graph diffusion for text-driven human motion generation. In *BMVC*, pp. 722–729, 2023. 3
- Lin Liu, Lingxi Xie, Xiaopeng Zhang, Shanxin Yuan, Xiangyu Chen, Wengang Zhou, Houqiang Li, and Qi Tian. Tape: Task-agnostic prior embedding for image restoration. In *ECCV*, 2022. 8

- Yun-Fu Liu, Da-Wei Jaw, Shih-Chia Huang, and Jenq-Neng Hwang. Desnownet: Context-aware deep network for snow removal. *TIP*, 27(6):3064–3073, 2018. 1
- Ziwei Luo, Fredrik K Gustafsson, Zheng Zhao, Jens Sjölund, and Thomas B Schön. Image restoration with mean-reverting stochastic differential equations. *arXiv preprint arXiv:2301.11699*, 2023. 3
- Ziwei Luo, Fredrik K Gustafsson, Zheng Zhao, Jens Sjölund, and Thomas B Schön. Controlling vision-language models for universal image restoration. In *ICLR*, 2024. 8
- Kede Ma, Zhengfang Duanmu, Qingbo Wu, Zhou Wang, Hongwei Yong, Hongliang Li, and Lei Zhang. Waterloo exploration database: New challenges for image quality assessment models. *IEEE TIP*, 26(2):1004–1016, 2016. 1
- David Martin, Charless Fowlkes, Doron Tal, and Jitendra Malik. A database of human segmented natural images and its application to evaluating segmentation algorithms and measuring ecological statistics. In *ICCV*, pp. 416–423, 2001. 1
- Chong Mou, Qian Wang, and Jian Zhang. Deep generalized unfolding networks for image restoration. In *CVPR*, pp. 17399–17410, 2022. 8
- Seungjun Nah, Tae Hyun Kim, and Kyoung Mu Lee. Deep multi-scale convolutional neural network for dynamic scene deblurring. In *CVPR*, pp. 3883–3891, 2017. 1
- Tam Minh Nguyen, Tan Minh Nguyen, Dung DD Le, Duy Khuong Nguyen, Viet-Anh Tran, Richard Baraniuk, Nhat Ho, and Stanley Osher. Improving transformers with probabilistic attention keys. In *ICML*, pp. 16595–16621. PMLR, 2022a. 5
- Tan Nguyen, Tam Nguyen, Hai Do, Khai Nguyen, Vishwanath Saragadam, Minh Pham, Khuong Duy Nguyen, Nhat Ho, and Stanley Osher. Improving transformer with an admixture of attention heads. *NeurIPS*, 35:27937–27952, 2022b. 5
- OpenAI. Introducing chatgpt. <https://openai.com/blog/chatgpt>, 2022. 11
- OpenAI. Gpt-4 technical report, 2023. 11
- Ozan Özdenizci and Robert Legenstein. Restoring vision in adverse weather conditions with patch-based denoising diffusion models. *TPAMI*, 45(8):10346–10357, 2023. 7, 9
- Vaishnav Potlapalli, Syed Waqas Zamir, Salman H Khan, and Fahad Shahbaz Khan. Promptir: Prompting for all-in-one image restoration. *NeurIPS*, 36, 2024. 2, 3, 7, 8, 9, 1, 4, 10
- Rui Qian, Robby T Tan, Wenhan Yang, Jiajun Su, and Jiaying Liu. Attentive generative adversarial network for raindrop removal from a single image. In *CVPR*, pp. 2482–2491, 2018. 1
- Yanyun Qu, Yizi Chen, Jingying Huang, and Yuan Xie. Enhanced pix2pix dehazing network. In *CVPR*, pp. 8160–8168, 2019. 3
- Bin Ren, Yahui Liu, Yue Song, Wei Bi, Rita Cucchiara, Nicu Sebe, and Wei Wang. Masked jigsaw puzzle: A versatile position embedding for vision transformers. In *CVPR*, pp. 20382–20391, 2023. 3
- Bin Ren, Yawei Li, Jingyun Liang, Rakesh Ranjan, Mengyuan Liu, Rita Cucchiara, Luc V Gool, Ming-Hsuan Yang, and Nicu Sebe. Sharing key semantics in transformer makes efficient image restoration. *NeurIPS*, 37:7427–7463, 2024. 2
- Bin Ren, Eduard Zamfir, Zongwei Wu, Yawei Li, Yidi Li, Danda Pani Paudel, Radu Timofte, Ming-Hsuan Yang, Luc Van Gool, and Nicu Sebe. Any image restoration via efficient spatial-frequency degradation adaptation. *TMLR*, 2026. 3, 2
- Wenqi Ren, Si Liu, Hua Zhang, Jinshan Pan, Xiaochun Cao, and Ming-Hsuan Yang. Single image dehazing via multi-scale convolutional neural networks. In *ECCV*, pp. 154–169, 2016. 3
- William Hadley Richardson. Bayesian-based iterative method of image restoration. *Journal of the Optical Society of America*, 62(1):55–59, 1972. 3

- Yuan Shi, Bin Xia, Xiaoyu Jin, Xing Wang, Tianyu Zhao, Xin Xia, Xuefeng Xiao, and Wenming Yang. Vmambair: Visual state space model for image restoration. *TSCVT*, 2025. 3
- Shangquan Sun, Wenqi Ren, Xinwei Gao, Rui Wang, and Xiaochun Cao. Restoring images in adverse weather conditions via histogram transformer. In *ECCV*, volume 15080, pp. 111–129, 2024. 8, 9, 2
- Aiqiang Tang, Yan Wu, and Yuwei Zhang. Ramir: Reasoning and action prompting with mamba for all-in-one image restoration. *Applied Intelligence*, 55(4):258, 2025a. 3, 8
- Xiaole Tang, Xiang Gu, Xiaoyi He, Xin Hu, and Jian Sun. Degradation-aware residual-conditioned optimal transport for unified image restoration. *TPAMI*, 2025b. 2, 3, 7, 8
- Chunwei Tian, Yong Xu, and Wangmeng Zuo. Image denoising using deep cnn with batch renormalization. *Neural Networks*, 2020. 8, 4
- Xiangpeng Tian, Xiangyu Liao, Xiao Liu, Meng Li, and Chao Ren. Degradation-aware feature perturbation for all-in-one image restoration. In *CVPR*, pp. 28165–28175, 2025. 3
- Zhengzhong Tu, Hossein Talebi, Han Zhang, Feng Yang, Peyman Milanfar, Alan Bovik, and Yinxiao Li. MAXIM: Multi-axis mlp for image processing. In *CVPR*, pp. 5769–5780, 2022. 3
- Jeya Maria Jose Valanarasu, Rajeev Yasarla, and Vishal M. Patel. Transweather: Transformer-based restoration of images degraded by adverse weather conditions. In *CVPR*, pp. 2343–2353, 2022. 8, 9, 1
- Shashanka Venkataramanan, Amir Ghodrati, Yuki M Asano, Fatih Porikli, and Amirhossein Habibian. Skip-attention: Improving vision transformers by paying less attention. In *ICLR*, 2024. 2, 5
- Cong Wang, Jinshan Pan, Wei Wang, Jiangxin Dong, Mengzhu Wang, Yakun Ju, and Junyang Chen. Promptrestorer: A prompting image restoration method with degradation perception. *NeurIPS*, 36: 8898–8912, 2023a. 3
- Huadong Wang, Xin Shen, Mei Tu, Yimeng Zhuang, and Zhiyuan Liu. Improved transformer with multi-head dense collaboration. *TASLP*, 30:2754–2767, 2022. 5
- Tao Wang, Kaihao Zhang, Ziqian Shao, Wenhan Luo, Bjorn Stenger, Tong Lu, Tae-Kyun Kim, Wei Liu, and Hongdong Li. Gridformer: Residual dense transformer with grid structure for image restoration in adverse weather conditions. *IJCV*, 132(10):4541–4563, 2024. 9
- Xintao Wang, Ke Yu, Chao Dong, and Chen Change Loy. Recovering realistic texture in image super-resolution by deep spatial feature transform. In *CVPR*, pp. 606–615, 2018. 3
- Yinhui Wang, Jiwen Yu, and Jian Zhang. Zero-shot image restoration using denoising diffusion null-space model. *ICLR*, 2023b. 3
- Chen Wei, Wenjing Wang, Wenhan Yang, and Jiaying Liu. Deep retinex decomposition for low-light enhancement. *arXiv preprint arXiv:1808.04560*, 2018. 1
- Wei Wei, Deyu Meng, Qian Zhao, Zongben Xu, and Ying Wu. Semi-supervised transfer learning for image rain removal. In *CVPR*, pp. 3877–3886, 2019. 4
- Gang Wu, Junjun Jiang, Kui Jiang, and Xianming Liu. Harmony in diversity: Improving all-in-one image restoration via multi-task collaboration. In *Proceedings of the 32nd ACM International Conference on Multimedia*, pp. 6015–6023, 2024. 8
- Haiyan Wu, Yanyun Qu, Shaohui Lin, Jian Zhou, Ruizhi Qiao, Zhizhong Zhang, Yuan Xie, and Lizhuang Ma. Contrastive learning for compact single image dehazing. In *CVPR*, pp. 10551–10560, 2021. 3
- Da Xiao, Qingye Meng, Shengping Li, and Xingyuan Yuan. Improving transformers with dynamically composable multi-head attention. In *ICML*, pp. 54300–54318. PMLR, 2024. 5
- Chengxing Xie, Xiaoming Zhang, Linze Li, Yuqian Fu, Biao Gong, Tianrui Li, and Kai Zhang. Mat: Multi-range attention transformer for efficient image super-resolution. *TSCVT*, 2025. 3

- Fuzhi Yang, Huan Yang, Jianlong Fu, Hongtao Lu, and Baining Guo. Learning texture transformer network for image super-resolution. In *CVPR*, pp. 5791–5800, 2020. 1
- Mingde Yao, Ruikang Xu, Yuanshen Guan, Jie Huang, and Zhiwei Xiong. Neural degradation representation learning for all-in-one image restoration. *TIP*, 2024. 8
- Rajeev Yasarla and Vishal M Patel. Uncertainty guided multi-scale residual learning-using a cycle spinning cnn for single image de-raining. In *CVPR*, pp. 8405–8414, 2019. 4
- Tian Ye, Sixiang Chen, Jinbin Bai, Jun Shi, Chenghao Xue, Jingxia Jiang, Junjie Yin, Erkang Chen, and Yun Liu. Adverse weather removal with codebook priors. In *ICCV*, pp. 12619–12630, 2023. 9
- Tian Ye, Sixiang Chen, Wenhao Chai, Zhaohu Xing, Jing Qin, Ge Lin, and Lei Zhu. Learning diffusion texture priors for image restoration. In *CVPR*, pp. 2524–2534, 2024. 9
- Zongsheng Yue, Jianyi Wang, and Chen Change Loy. ResShift: Efficient diffusion model for image super-resolution by residual shifting. *arXiv preprint arXiv:2307.12348*, 2023. 3
- Eduard Zamfir, Zongwei Wu, Nancy Mehta, Yulun Zhang, and Radu Timofte. See more details: Efficient image super-resolution by experts mining. In *ICML*. PMLR, 2024. 3
- Eduard Zamfir, Zongwei Wu, Nancy Mehta, Yuedong Tan, Danda Pani Paudel, Yulun Zhang, and Radu Timofte. Complexity experts are task-discriminative learners for any image restoration. In *CVPR*, 2025. 2, 3, 7, 8, 9, 1, 10
- Syed Waqas Zamir, Aditya Arora, Salman Khan, Munawar Hayat, Fahad Shahbaz Khan, Ming-Hsuan Yang, and Ling Shao. Multi-stage progressive image restoration. In *CVPR*, pp. 14821–14831, 2021. 8
- Syed Waqas Zamir, Aditya Arora, Salman Khan, Munawar Hayat, Fahad Shahbaz Khan, and Ming-Hsuan Yang. Restormer: Efficient transformer for high-resolution image restoration. In *CVPR*, pp. 5728–5739, 2022. 2, 3, 8, 9
- Haijin Zeng, Xiangming Wang, Yongyong Chen, Jingyong Su, and Jie Liu. Vision-language gradient descent-driven all-in-one deep unfolding networks. In *CVPR*, 2025. 3, 7, 8
- Lujun Zhai, Yonghui Wang, Suxia Cui, and Yu Zhou. A comprehensive review of deep learning-based real-world image restoration. *Access*, 11:21049–21067, 2023. 4
- He Zhang and Vishal M Patel. Density-aware single image de-raining using a multi-stream dense network. In *CVPR*, pp. 695–704, 2018. 4
- Jinghao Zhang, Jie Huang, Mingde Yao, Zizheng Yang, Hu Yu, Man Zhou, and Feng Zhao. Ingredient-oriented multi-degradation learning for image restoration. In *CVPR*, pp. 5825–5835, 2023. 3, 7, 8, 9
- Kai Zhang, Wangmeng Zuo, Yunjin Chen, Deyu Meng, and Lei Zhang. Beyond a gaussian denoiser: Residual learning of deep cnn for image denoising. *IEEE TIP*, 26(7):3142–3155, 2017a. 3, 4
- Kai Zhang, Wangmeng Zuo, Shuhang Gu, and Lei Zhang. Learning deep cnn denoiser prior for image restoration. In *CVPR*, pp. 3929–3938, 2017b. 3, 4
- Kai Zhang, Wangmeng Zuo, and Lei Zhang. FFDNet: Toward a fast and flexible solution for cnn-based image denoising. *IEEE TIP*, 27(9):4608–4622, 2018. 4
- Leheng Zhang, Yawei Li, Xingyu Zhou, Xiaorui Zhao, and Shuhang Gu. Transcending the limit of local window: Advanced super-resolution transformer with adaptive token dictionary. *arXiv preprint arXiv:2401.08209*, 2024. 3
- Xu Zhang, Jiaqi Ma, Guoli Wang, Qian Zhang, Huan Zhang, and Lefei Zhang. Perceive-ir: Learning to perceive degradation better for all-in-one image restoration. *TIP*, 2025. 3
- Yulun Zhang, Kunpeng Li, Kai Li, Bineng Zhong, and Yun Fu. Residual non-local attention networks for image restoration. *arXiv preprint arXiv:1903.10082*, 2019. 3

- Mengyi Zhao, Mengyuan Liu, Bin Ren, Shuling Dai, and Nicu Sebe. Denoising diffusion probabilistic models for action-conditioned 3d motion generation. In *ICASSP*, pp. 4225–4229. IEEE, 2024. 3
- Dian Zheng, Xiao-Ming Wu, Shuzhou Yang, Jian Zhang, Jian-Fang Hu, and Wei-Shi Zheng. Selective hourglass mapping for universal image restoration based on diffusion model. In *CVPR*, pp. 25445–25455, 2024a. 7
- Xu Zheng, Yuanhuiyi Lyu, and Lin Wang. Learning modality-agnostic representation for semantic segmentation from any modalities. In *ECCV*, pp. 146–165. Springer, 2024b. 3
- Yuqian Zhou, David Ren, Neil Emerton, Sehoon Lim, and Timothy Large. Image restoration for under-display camera. In *Proceedings of the IEEE/CVF conference on computer vision and pattern recognition*, pp. 9179–9188, 2021. 7
- Lianghui Zhu, Bencheng Liao, Qian Zhang, Xinlong Wang, Wenyu Liu, and Xinggang Wang. Vision mamba: Efficient visual representation learning with bidirectional state space model. *arXiv preprint arXiv:2401.09417*, 2024. 3
- Yurui Zhu, Tianyu Wang, Xueyang Fu, Xuanyu Yang, Xin Guo, Jifeng Dai, Yu Qiao, and Xiaowei Hu. Learning weather-general and weather-specific features for image restoration under multiple adverse weather conditions. In *CVPR*, pp. 21747–21758, 2023. 7, 8, 9, 1

A EXPERIMENTAL PROTOCOLS

A.1 DATASETS

3 Degradation Datasets. For both the All-in-One and single-task settings, we follow the evaluation protocols established in prior works [Li et al. \(2022\)](#); [Potlapalli et al. \(2024\)](#); [Zamfir et al. \(2025\)](#), utilizing the following datasets: For image denoising in the single-task setting, we combine the BSD400 [Arbelaez et al. \(2010\)](#) and WED [Ma et al. \(2016\)](#) datasets, and corrupt the images with Gaussian noise at levels $\sigma \in \{15, 25, 50\}$. BSD400 contains 400 training images, while WED includes 4,744 images. We evaluate the denoising performance on BSD68 [Martin et al. \(2001\)](#) and Urban100 [Huang et al. \(2015\)](#). For single-task deraining, we use Rain100L [Yang et al. \(2020\)](#), which provides 200 clean/rainy image pairs for training and 100 pairs for testing. For single-task dehazing, we adopt the SOTS dataset [Li et al. \(2018\)](#), consisting of 72,135 training images and 500 testing images. Under the All-in-One setting, we train a unified model on the combined set of the aforementioned training datasets for 120 epochs and directly test it across all three restoration tasks.

5 Degradation Datasets. The 5-degradation setting is built upon the 3-degradation setting, with two additional tasks included: deblurring and low-light enhancement. For deblurring, we adopt the GoPro dataset [Nah et al. \(2017\)](#), which contains 2,103 training images and 1,111 testing images. For low-light enhancement, we use the LOL-v1 dataset [Wei et al. \(2018\)](#), consisting of 485 training images and 15 testing images. Note that for the denoising task under the 5-degradation setting, we report results using Gaussian noise with $\sigma = 25$. The training takes 130 epochs.

Composited Degradation Datasets. Regarding the composite degradation setting, we use the CDD11 dataset [Guo et al. \(2024b\)](#). CDD11 consists of 1,183 training images for: (i) 4 kinds of single-degradation types: haze (H), low-light (L), rain (R), and snow (S); (ii) 5 kinds of double-degradation types: low-light + haze (L+H), low-light+rain (L+R), low-light + snow (L+S), haze + rain (H+R), and haze + snow (H+S). (iii) 2 kinds of Triple-degradation type: low-light + haze + rain (L+H+R), and low-light + haze + snow (L+H+S). We train our method for 170 epochs (fewer than 200 epochs than MoCE-IR [Zamfir et al. \(2025\)](#)), and we keep all other settings unchanged.

Adverse Weather Removal Datasets. For the deweathering tasks, we follow the experimental setups used in TransWeather [Valanarasu et al. \(2022\)](#) and WGWSNet [Zhu et al. \(2023\)](#), evaluating the performance of our approach on multiple synthetic datasets. We assess the capability of MIRAGE across three challenging tasks: snow removal, rain streak and fog removal, and raindrop removal. The training set, referred to as “AllWeather”, is composed of images from the Snow100K [Liu et al. \(2018\)](#), Raindrop [Qian et al. \(2018\)](#), and Outdoor-Rain [Li et al. \(2019b\)](#) datasets. For testing, we evaluate our model on the following subsets: Snow100K-S (16,611 images), Snow100K-L (16,801

Table A: The details our the tiny and small version of our MIRAGE . FLOPs are computed on an image of size 224×224 using a NVIDIA Tesla A100 (40G) GPU.

	MIRAGE -T	MIRAGE -S
The Number of the MDAB crosses 4 scales	[3, 5, 5, 7]	[3, 5, 5, 7]
The Input Embedding Dimension	24	30
The FFN Expansion Factor	2	2
The Number of the Refinement Blocks	2	3
Params. (\downarrow)	6.21M	9.68 M
FLOPs (\downarrow)	16 G	27 G

images), Outdoor-Rain (750 images), and Raindrop (249 images). Same as Histoformer [Sun et al. \(2024\)](#), we train MIRAGE on “AllWeather” with 300,000 iterations.

Zero-Shot Underwater Image Enhancement Dataset. For the zero-shot underwater image enhancement setting, we follow the evaluation protocol of DCPT [JiaKui et al. \(2025\)](#) by directly applying our model, trained under the 5-degradation setting, on the UIEB dataset [Li et al. \(2019a\)](#) without any finetuning. UIEB consists of two subsets: 890 raw underwater images with corresponding high-quality reference images, and 60 challenging underwater images. We evaluate our zero-shot performance on the 890-image subset with available reference images.

A.2 IMPLEMENTATION DETAILS

Implementation Details. Our MIRAGE framework is designed to be end-to-end trainable, removing the need for multi-stage optimization of individual components. The architecture adopts a robust 4-level encoder-decoder structure, with a varying number of Mixed Degradation Attention Blocks (MDAB) at each level—specifically [3, 5, 5, 7] from highest to lowest resolution in the Tiny variant. Following prior works [Potlapalli et al. \(2024\)](#); [Zamfir et al. \(2025\)](#), we train the model for 120 epochs with a batch size of 32 in both the 3-Degradation All-in-One and single-task settings. The optimization uses a combination of L_1 and Fourier loss, optimized with Adam [Kingma & Ba \(2015\)](#) (initial learning rate of 2×10^{-4} , $\beta_1 = 0.9$, $\beta_2 = 0.999$) and a cosine decay schedule. During training, we apply random cropping to 128×128 patches, along with horizontal and vertical flipping as data augmentation. All experiments are conducted on a single NVIDIA H200 GPU (140 GB). Memory usage is approximately 42 GB for the Tiny (*i.e.*, MIRAGE -T) model and 56 GB for the Small model (*i.e.*, MIRAGE -S).

Model Scaling. We propose two scaled variants of our MIRAGE , namely Tiny (MIRAGE -T) and Small (MIRAGE -S). As detailed in Tab. A, these variants differ in terms of the number of MDAB blocks across scales, the input embedding dimension, the FFN expansion factor, and the number of refinement blocks.

A.3 OPTIMIZATION OBJECTIVES

The overall optimization objective of our approach is defined as:

$$\mathcal{L}_{\text{total}} = \mathcal{L}_1 + \lambda_{fre} \times \mathcal{L}_{\text{Fourier}} + \lambda_{ctr s} \times \mathcal{L}_{\text{SPD}}. \quad (\text{A})$$

Here, $\mathcal{L}_{\text{Fourier}}$ denotes the real-valued Fourier loss computed between the restored image and the ground-truth image, and \mathcal{L}_{SPD} represents our proposed contrastive learning objective in the SPD (Symmetric Positive Definite) space.

Specifically, we adopt an ℓ_1 loss that adopted in IR tasks [Potlapalli et al. \(2024\)](#); [Zamfir et al. \(2025\)](#); [Li et al. \(2022\)](#); [Ren et al. \(2026\)](#); [Cui et al. \(2025\)](#); [Ren et al. \(2024\)](#); [Li et al. \(2025\)](#), defined as $\mathcal{L}_1 = \|\hat{x} - x\|_1$, to enforce pixel-wise similarity between the restored image \hat{x} and the ground-truth image x . $\mathcal{L}_{\text{Fourier}}$, as utilized in MoCE-IR [Zamfir et al. \(2025\)](#); [Cui et al. \(2025\)](#), to enhance frequency-domain consistency, the real-valued Fourier loss, is defined as:

$$\mathcal{L}_{\text{Fourier}} = \|\mathcal{F}_{\text{real}}(\hat{x}) - \mathcal{F}_{\text{real}}(x)\|_1 + \|\mathcal{F}_{\text{imag}}(\hat{x}) - \mathcal{F}_{\text{imag}}(x)\|_1, \quad (\text{B})$$

where \hat{x} and x denote the restored and ground-truth images, respectively. $\mathcal{F}_{\text{real}}(\cdot)$ and $\mathcal{F}_{\text{imag}}(\cdot)$ represent the real and imaginary parts of the 2D real-input FFT (*i.e.*, rfft2). The final loss is computed as the ℓ_1 distance between the real and imaginary components of the predicted and target frequency

spectra. Same as MoCE-IR [Zamfir et al. \(2025\)](#), λ_{fre} is set to 0.1 throughout our experiments. Meanwhile, the \mathcal{L}_{SPD} is defined as in Eq. 3-5 of our main manuscript. More ablation studies regarding the proposed \mathcal{L}_{SPD} are provided in Sec. C.3. The temperature parameter τ of the proposed \mathcal{L}_{SPD} is set to 0.1 throughout all the experiments.

B PRELIMINARIES ON SPD-BASED FEATURE STATISTICS

This section provides a brief background on the concepts involved in our cross-layer alignment strategy. The intention is to supply intuitive context—rather than additional derivations—for second-order feature statistics, the SPD structure, and depth-asymmetric representations used in Sec. 4.2.

Second-order feature statistics. Raw activations capture local appearance, but the way channels vary together often reveals more stable information about degradations. For a feature matrix $X \in \mathbb{R}^{C \times N}$, the covariance

$$\mathbf{C} = \frac{1}{N-1}(X - \mu)(X - \mu)^\top$$

summarizes inter-channel relationships. Diagonal entries reflect each channel’s variability, while off-diagonal entries describe redundancy and dependence patterns. These structures differ consistently across layers and degradations (Fig. 4; Appendix Fig. B), making covariance a compact and informative descriptor.

SPD property of covariance matrices. Covariance matrices are symmetric and positive definite by construction and therefore lie in the SPD set. This structure encodes meaningful geometric information: eigenvalues represent correlation strengths, and the matrix as a whole can be interpreted as a “shape” in channel space. Preserving this structure is important—direct Euclidean operations may flatten or distort correlation patterns, an effect also reflected in the collapse observed with Euclidean contrastive learning (Fig. 6).

Representing SPD matrices for comparison. To compare covariance matrices within a contrastive objective, we vectorize \mathbf{C} and apply a learnable projection. This retains second-order relationships while mapping them to an embedding space suitable for contrastive learning. Compared to raw feature vectors, covariance embeddings emphasize structural organization and therefore provide a more stable alignment signal.

Depth-asymmetric representations. Shallow and latent features naturally exhibit different statistical behavior: shallow layers respond strongly to local degradations and show pronounced redundancy, while deeper layers become more decorrelated and semantically aggregated. Their covariance matrices reflect these differences in a consistent way across degradations, making shallow–latent pairs complementary views of the same signal and a natural target for alignment.

Intuition behind SPD-based alignment. Aligning covariance-based SPD embeddings focuses on how channels interact, rather than on individual activation values. This yields supervision that is less sensitive to local noise and more reflective of the underlying representation structure. Encouraging shallow and latent features to share similar second-order statistics stabilizes the shared feature space required for diverse degradations.

Overall, covariance provides a compact view of channel interactions, the SPD structure preserves meaningful second-order relations, and depth-asymmetric covariance patterns naturally motivate the alignment strategy formalized in Sec. 4.2.

C MORE METHOD DETAILS & SUPPLEMENTARY EXPERIMENTS

C.1 1 DEG. COMPARISON

Single-Degradation. In Tab. B, we compare our method against state-of-the-art approaches on single degradation tasks. For dehazing on SOTS dataset, we compare with DehazeNet [Cai et al. \(2016\)](#), MSCNN [Ren et al. \(2016\)](#), AODNet [Li et al. \(2017\)](#), EPDN [Qu et al. \(2019\)](#), FDGAN [Dong et al. \(2020\)](#), and all-in-one methods AirNet [Li et al. \(2022\)](#) and PromptIR [Potlapalli et al. \(2024\)](#). Our 6M parameter model achieves competitive performance (31.46 dB PSNR, 0.977 SSIM), while our 10M model establishes new state-of-the-art results (31.53 dB PSNR, 0.980 SSIM), outperforming the much

Table B: Comparison to state-of-the-art for single degradations. PSNR (dB, \uparrow) and SSIM (\uparrow) metrics are reported on the full RGB images. **Best** performance is highlighted. Our method excels over prior works.

(a) Dehazing			(b) Deraining			(c) Denoising on BSD68				
Method	Params.	SOTS	Method	Params.	Rain100L	Method	Params.	$\sigma=15$	$\sigma=25$	$\sigma=50$
DehazeNet	-	22.46 .851	DIDMDN	-	23.79 .773	DnCNN	-	33.89 .930	31.23 .883	27.92 .789
MSCNN	-	22.06 .908	UMR	-	32.39 .921	IRCNN	-	33.87 .929	31.18 .882	27.88 .790
AODNet	-	20.29 .877	SIRR	-	32.37 .926	FFDNet	-	33.87 .929	31.21 .882	27.96 .789
EPDN	-	22.57 .863	MSPFN	-	33.50 .948	BRDNet	-	34.10 .929	31.43 .885	28.16 .794
FDGAN	-	23.15 .921	LPNet	-	23.15 .921	AirNet	9M	34.14 .936	31.48 .893	28.23 .806
AirNet	9M	23.18 .900	AirNet	9M	34.90 .977	PromptIR	36M	34.34 .938	31.71 .897	28.49 .813
PromptIR	36M	31.31 .973	PromptIR	36M	37.04 .979	PromptIR (Reproduce)	36M	34.15 .934	31.50 .894	28.33 .807
MIRAGE (Ours)	6M	31.46 .977	MIRAGE (ours)	6M	37.47 .980	MIRAGE (ours)	6M	34.23 .936	31.60 .896	28.36 .808
MIRAGE (Ours)	10M	31.53 .980	MIRAGE (Ours)	10M	38.01 .982	MIRAGE (Ours)	10M	34.25 .937	31.65 .898	28.38 .810

Algorithm A DynamicDepthwiseConv

Require: $\alpha \in \mathbb{R}^{B \times C \times H \times W}$ ▷ Input feature map
Ensure: $\alpha' \in \mathbb{R}^{B \times C \times H \times W}$ ▷ Output after dynamic depthwise conv

[Step 1] Generate Dynamic Kernel

- 1: $K \leftarrow \text{AdaptiveAvgPool2D}(\alpha)$ ▷ Global context pooling
- 2: $K \leftarrow \text{Conv2D}(K, 1 \times 1, \text{out_ch} = C)$ ▷ Linear projection
- 3: $K \leftarrow \text{GELU}(K)$ ▷ Non-linear activation
- 4: $K \leftarrow \text{Conv2D}(K, 1 \times 1, \text{out_ch} = C \cdot k^2)$ ▷ Generate kernel weights
- 5: $K \leftarrow \text{Reshape}(K, [B \cdot C, 1, k, k])$ ▷ Form depthwise filters

[Step 2] Apply Depthwise Convolution

- 6: $\alpha_{\text{flat}} \leftarrow \text{Reshape}(\alpha, [1, B \cdot C, H, W])$ ▷ Prepare for grouped conv
- 7: $\alpha'_{\text{flat}} \leftarrow \text{Conv2D}(\alpha_{\text{flat}}, K, \text{groups} = B \cdot C, \text{padding} = k \div 2)$ ▷ Apply dynamic depthwise conv
- 8: $\alpha' \leftarrow \text{Reshape}(\alpha'_{\text{flat}}, [B, C, H, W])$ ▷ Reshape back to original shape
- 9: **return** α'

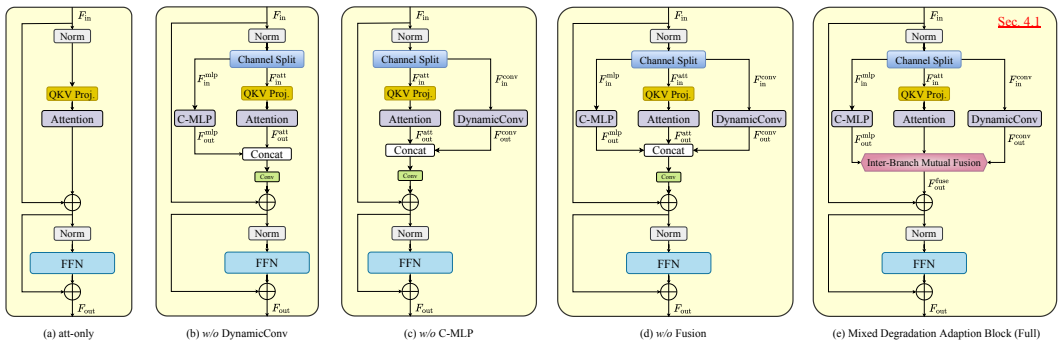


Figure A: The illustration of different designs of the proposed MDAB.

larger PromptIR (36M parameters). For deraining on Rain100L, we evaluate against DIDMDN Zhang & Patel (2018), UMR Yasarla & Patel (2019), SIRR Wei et al. (2019), MSPFN Jiang et al. (2020), LPNet Gao et al. (2019), AirNet Li et al. (2022), and PromptIR Potlapalli et al. (2024). Our method significantly outperforms all baselines, with our 10M model achieving 38.01 dB PSNR and 0.982 SSIM. For denoising on BSD68, we compare with classical methods DnCNN Zhang et al. (2017a), IRCNN Zhang et al. (2017b), FFDNet Zhang et al. (2018), BRDNet Tian et al. (2020), and recent all-in-one approaches AirNet Li et al. (2022) and PromptIR Potlapalli et al. (2024). Our method consistently outperforms all competitors across different noise levels ($\sigma=15, 25, 50$), demonstrating superior performance with significantly fewer parameters than existing all-in-one methods.

Algorithm B SPD Contrastive Learning Optimization Pseudocode

```

# fen: encoder
# fde: decoder
# patch_embedding: shallow convolutional patch embedding
# refinement_conv: the refinement block and the final convolution
# spd: compute SPD feature
for x in loader: # load a minibatch x with n samples

    Fshallow = patch_embedding(x) # Convolutional Patch Embedding
    Flatent = fen(Fshallow)

    Cs, Cl = spd(Fshallow), spd(Flatent) # Compute SPD (Symmetric Positive Definite)
    manifold features
    zs, zl = proj_norm(Cs), proj_norm(Cl) # Projection and normalize

    Frecon = fde(Flatent)
    x̂ = refinement_conv(Frecon)

    L = L1(x, x̂) + λfre × LFourier(x, x̂) + λctr × LSPD(zs, zl) # total loss

    L.backward() # back-propagate
    update(fen, fde, patch_embedding, refinement_conv) # SGD update

def LFourier(a, b): # Real-valued Fourier loss
    Please refer to Eq.B of our Appendix.
    return loss

def LSPD(a, b): # SPD Loss
    Please refer to Eq.5 of our main manuscript.
    return loss

```

C.2 DETAILS OF THE DESIGN FOR THE PROPOSED MIXED BACKBONE.

To investigate the effectiveness of combining MLP, convolution, and attention mechanisms, we conducted an extensive design-level ablation study. The quantitative results are presented in Tab. 7 of the main manuscript. Here, we provide detailed visual illustrations of each design in Fig. A.

C-MLP. To strengthen channel-wise representation, we introduce a Channel-wise MLP module, denoted as C-MLP(). Given the input feature map $F_{in}^{mlp} \in \mathbb{R}^{B \times C \times H \times W}$, we first flatten the spatial dimensions to obtain a sequence $F_{in}^{mlp} \in \mathbb{R}^{B \times C \times L}$, where $L = H \times W$. The C-MLP is implemented using two 1D convolutional layers with a GELU activation in between. The GELU function introduces non-linearity, enabling the model to learn more complex and expressive channel-wise transformations. After processing, the output is reshaped back to the original spatial format, yielding $F_{out}^{mlp} \in \mathbb{R}^{B \times C \times H \times W}$.

Dynamic Depthwise Convolution. The DynamicDepthwiseConv() module is designed to capture content-adaptive local structures and is employed in Alg.1 of our main manuscript. As detailed in Alg. A, the input feature $\alpha \in \mathbb{R}^{B \times C \times H \times W}$ is first passed through a global average pooling and two 1×1 convolutions to generate a dynamic depthwise kernel for each channel and sample. The input is reshaped and convolved with the generated kernels using grouped convolution, enabling sample-specific spatial filtering. The resulting output α' maintains the original resolution while embedding adaptive local information.

C.3 DETAILS OF THE PROPOSED SPD CONTRASTIVE LEARNING.

As shown in Alg. B, our SPD-based contrastive learning aims to align shallow and latent representations by operating in the space of symmetric positive definite (SPD) matrices. Specifically, given the shallow features extracted from the convolutional patch embedding and the latent features produced by the encoder, we compute their second-order channel-wise statistics to obtain SPD representations. These matrices are then vectorized and projected through learnable MLP layers, followed by ℓ_2 normalization to form contrastive embeddings. An InfoNCE-style loss is applied between the shallow and latent embeddings to encourage structural alignment across depth. This contrastive term complements the pixel-level and frequency-based objectives, promoting more discriminative and consistent feature learning without introducing any additional cost during inference. Importantly,

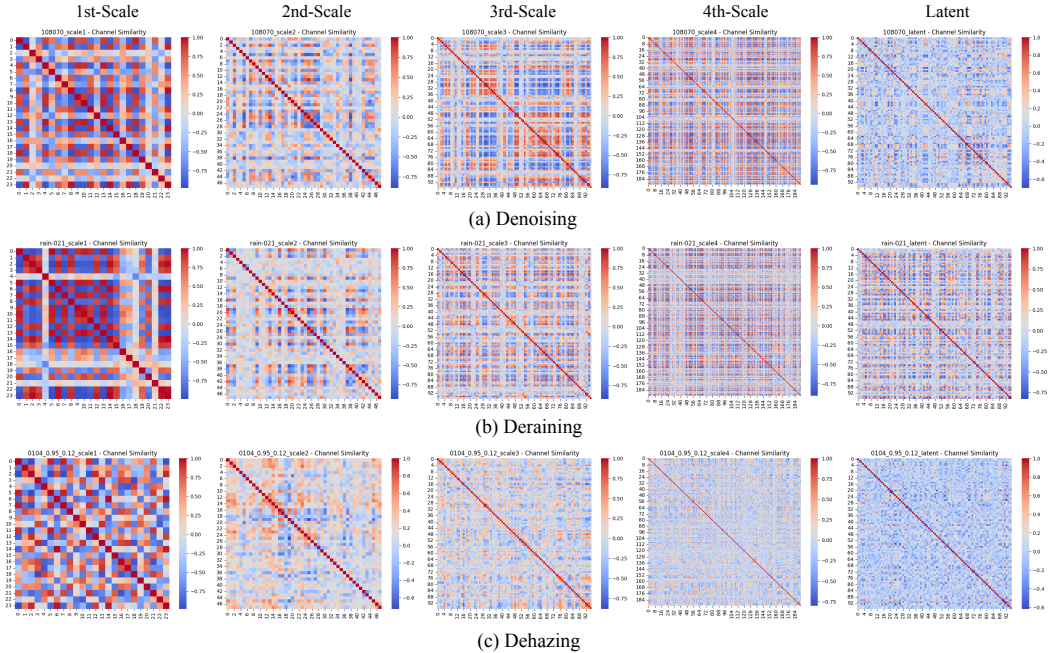


Figure B: The cross-scale channel-wise similarity matrix visualization for Denoising, Deraining, and Dehazing.

by leveraging the geometry of second-order feature statistics, our approach implicitly regularizes the representation space, encouraging intra-instance compactness and inter-degradation separability. This geometrically grounded formulation bridges low-level signal priors with high-level contrastive learning, offering a principled and scalable solution to all-in-one image restoration.

C.4 ABLATION REGARDING THE OPTIMIZATION OBJECTIVES

Tab. C shows that replacing SPD-based contrastive learning with a standard Euclidean-space contrastive loss (*w/o SPD*) results in a clear performance drop, demonstrating the advantage of modeling second-order channel correlations on the SPD manifold rather than relying solely on first-order vector similarities. When the entire contrastive module is removed (*w/o CL & SPD*), performance degrades even further, indicating that aligning shallow and deep features is essential for effective representation learning. Moreover, removing the Fourier loss (*w/o Fourier Loss*) slightly reduces performance, suggesting that frequency-domain supervision provides additional benefits. Overall, the full model achieves the best results, confirming the effectiveness of jointly optimizing spatial, frequency, and SPD-manifold-based structural consistency. Note that throughout all the experiments, we set $\lambda_{ctrls} = 0.05$ and $\lambda_{ctrls} = 0.1$.

Table C: Ablation Study of MIRAGE -T on 3 Degradation Setting.

Ablaton	Parms.	Results	
		PSNR (dB, \uparrow)	SSIM (\downarrow)
<i>w/o CL & SPD</i>	5.80M	32.63 (-0.14)	.916
<i>w/o SPD</i>	6.10M	32.53 (-0.24)	.914
<i>w/o Fourier Loss</i>	5.80M	32.70 (-0.07)	.917
MIRAGE -T (Full)	6.21M	32.77	.919

C.5 SHALLOW-LATENT FEATURE SIMILARITY

Besides the channel-wise similarity comparison provided in our main manuscript for denoising. We also find consistent findings in other degradation, *i.e.*, raining and hazing. The corresponding channel-wise similarity across scales is provided in Fig. B. These observations reveal several important trends: (i) Despite the diversity of degradation types, a consistent pattern emerges across scales. Specifically, from the first to the fourth scale, the overall channel-wise similarity indicates substantial redundancy among feature channels. After channel reduction, the latent features become more decorrelated, which validates the rationale for applying contrastive learning between the latent and shallow (*i.e.*, first-scale) features. (ii) Different degradation types exhibit varying degrees of channel redundancy.

Table D: Zero-shot evaluation on real-world under-display camera datasets TOLED and POLED (Zhou et al., 2021).

Method	TOLED (PSNR / SSIM / LPIPS)	POLED (PSNR / SSIM / LPIPS)
AirNet (Li et al., 2022)	14.58 / 0.609 / 0.445	7.53 / 0.350 / 0.820
PromptIR (Potlapalli et al., 2024)	16.70 / 0.688 / 0.422	13.16 / 0.583 / 0.619
DiffUIR (Zheng et al., 2024a)	29.55 / 0.887 / 0.281	15.62 / 0.424 / 0.505
MIRAGE-S (Ours)	28.01 / 0.881 / 0.293	16.93 / 0.604 / 0.500

As illustrated in Fig. B, hazy images tend to produce more inherently independent features, whereas rain-degraded inputs show strong channel-wise redundancy even in the latent space. This suggests that degradations like haze may benefit from larger embedding dimensions to capture more expressive representations, while simpler degradations (*e.g.*, rain) can achieve effective restoration with smaller embedding sizes due to their inherently redundant structure.

These insights open up new directions for adaptive and degradation-aware model design in future research. Notably, this trend is not limited to the three representative samples shown; we observe similar patterns consistently across the dataset in a statistical sense. We plan to conduct a more comprehensive and quantitative investigation of this phenomenon in future work.

C.6 MORE GENERALIZATION EVALUATION

To further assess generalization beyond synthetic settings, we evaluate MIRAGE-S on the real-world TOLED and POLED under-display camera datasets (Zhou et al., 2021). As shown in Tab. D, MIRAGE-S achieves strong performance across both benchmarks. On POLED, which contains more severe signal attenuation and non-linear spatial artifacts, MIRAGE-S clearly surpasses prior methods across all three metrics, indicating robust transfer to challenging real-world degradations. On TOLED, MIRAGE-S remains competitive and delivers results close to diffusion-based DiffUIR despite its significantly lower complexity. These findings suggest that the proposed mixed-backbone architecture and SPD-based alignment maintain good stability under real sensor degradations and generalize reliably across distinct UDC hardware conditions.

D ADDITIONAL VISUAL RESULTS.

D.1 3 DEGRADATION

Fig. C presents qualitative comparisons on representative cases of denoising, deraining, and dehazing, benchmarked against recent state-of-the-art methods. The proposed MIRAGE consistently yields more visually faithful restorations, characterized by enhanced structural integrity, finer texture details, and reduced artifacts. These results underscore the effectiveness of our unified framework in handling diverse degradation types while preserving high-frequency information and geometric consistency.

D.2 5 DEGRADATION

For the 5-degradation setting, we provide visual comparisons for the low-light enhancement task in Fig. D. As illustrated, the proposed MIRAGE produces noticeably cleaner outputs with improved luminance restoration and better color consistency compared to MoCE-IR Zamfir et al. (2025), demonstrating its robustness under challenging illumination conditions.

D.3 COMPOSITED DEGRADATION

Fig. E and Fig. F present visual comparisons under more challenging composite degradations, namely *low-light + haze + snow* and *low-light + haze + rain*, respectively. As observed, our method reconstructs significantly more scene details and preserves structural consistency, whereas MoCE-IR Zamfir et al. (2025) tends to produce noticeable artifacts and over-smoothed regions under these complex conditions.

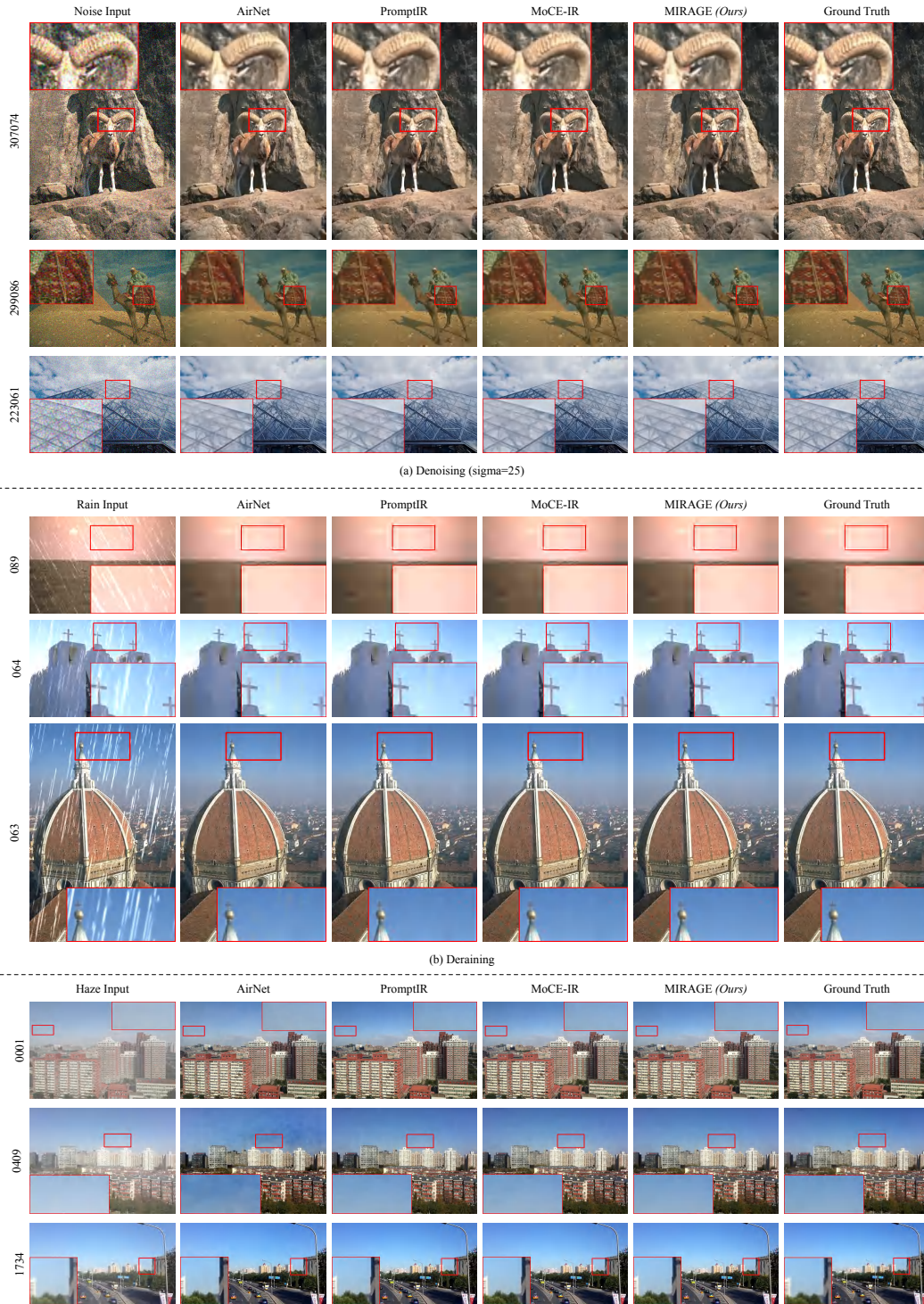


Figure C: Visual comparison of MIRAGE with state-of-the-art methods considering three degradations. Zoom in for a better view.

D.4 ZERO-SHOT UNDERWATER IMAGE ENHANCEMENT

Fig. G demonstrates that even when directly applied to unseen underwater images, our method is able to effectively enhance visibility and contrast, producing results that are noticeably clearer than the

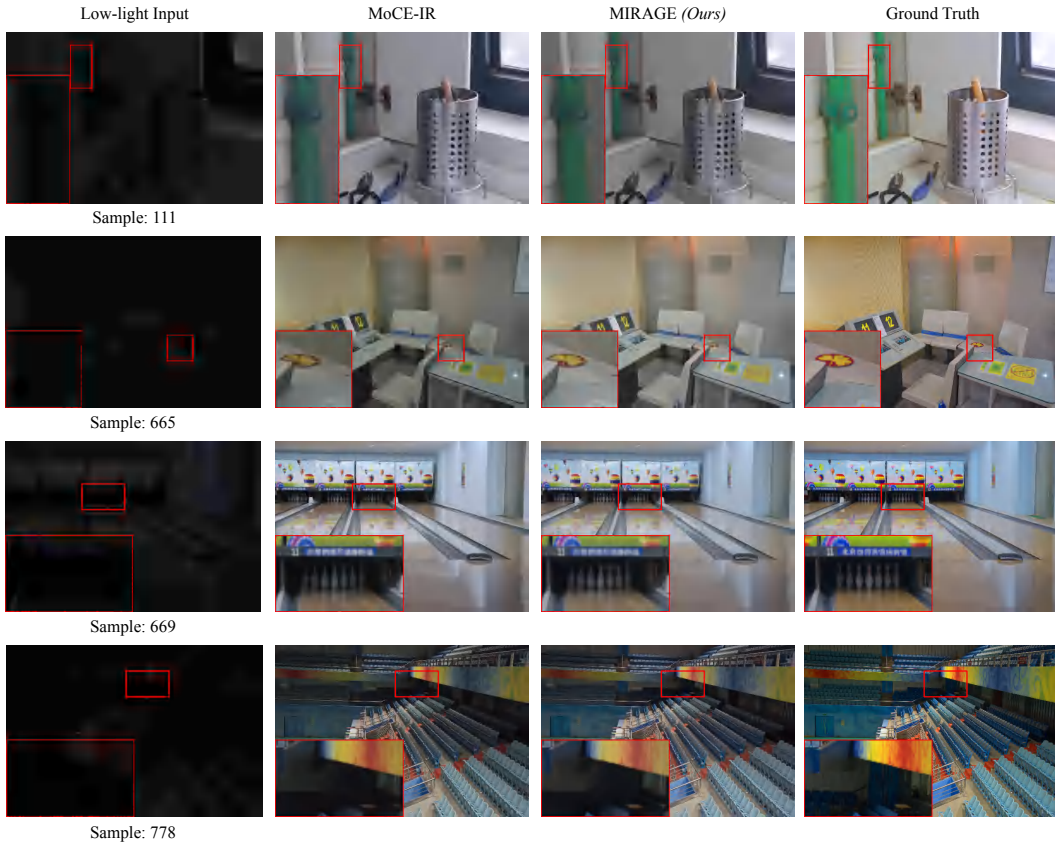


Figure D: Visual comparison of MIRAGE with state-of-the-art methods considering low-light degradation. Zoom in for a better view.



Figure E: Visual comparison of MIRAGE with state-of-the-art methods considering composited degradation (Low-light + Haze + Snow). Zoom in for a better view.

raw input and visually closer to the reference images. This qualitative evidence further validates the strong generalization ability of the proposed framework to unseen domains.

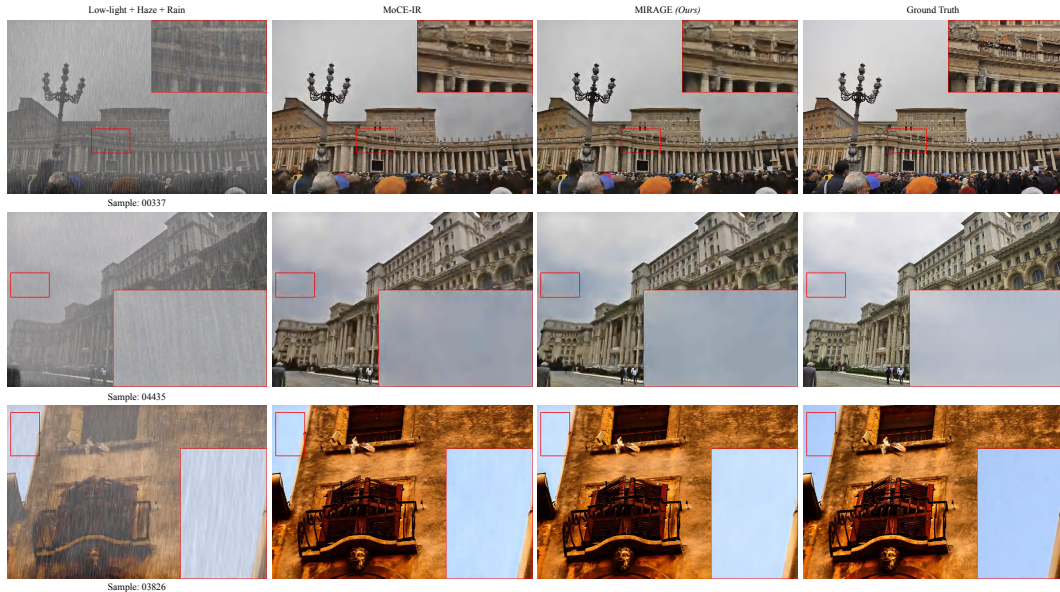


Figure F: Visual comparison of MIRAGE with state-of-the-art methods considering composited degradation (Low-light + Haze + Rain). Zoom in for a better view.

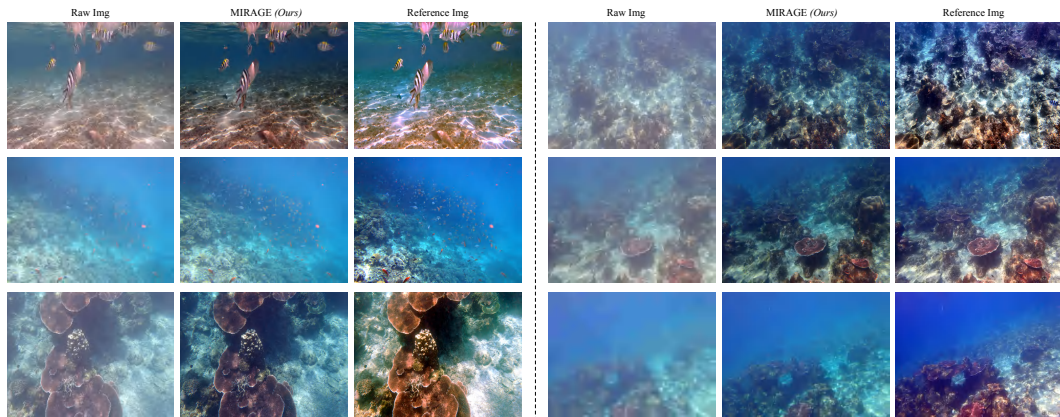


Figure G: Visual results of MIRAGE for Underwater Image Enhancement. Zoom in for a better view.

E LIMITATIONS AND FUTURE WORK

While the proposed MIRAGE achieves new state-of-the-art performance on most all-in-one image restoration benchmarks, we observe that its deblurring performance still lags slightly behind MoCE-IR [Zamfir et al. \(2025\)](#). We attribute this to the relatively compact model size of our current design, which favors efficiency over aggressive capacity. To address this, future work will explore scaling up the model size to be on par with larger architectures such as PromptIR [Potlapalli et al. \(2024\)](#), MoCE-IR [Zamfir et al. \(2025\)](#), and AdaIR [Cui et al. \(2025\)](#), aiming to further boost performance while maintaining the architectural elegance and efficiency of our design. Moreover, our current SPD-based contrastive learning leverages a conventional InfoNCE loss in Euclidean space after projecting SPD features. While effective, it does not fully exploit the intrinsic geometry of the SPD manifold. As part of future efforts, we plan to investigate geodesic-based contrastive formulations and Riemannian-aware optimization strategies, which may offer a more principled and theoretically grounded way to align structured representations across semantic scales. Additionally, different degradations may favor different proportions of convolution, attention, and MLP capacity. Learning such ratios dynamically is an interesting direction and could further adapt MIRAGE to degradation-specific characteristics. We view this as a promising avenue for future research.

F BROADER IMPACT

Image restoration (IR) is a fundamental task with applications in photography, remote sensing, surveillance, autonomous driving, medical imaging, and scientific visualization. By proposing a unified and efficient framework capable of handling diverse degradation types with minimal computational cost, our work may benefit scenarios where image quality is compromised by environmental or hardware constraints. The lightweight design of MIRAGE further enables deployment on resource-limited devices such as mobile phones, drones, or embedded cameras, which can support use cases in low-resource settings or critical domains like emergency response and environmental monitoring. From a research perspective, our modular design and SPD-based contrastive formulation may encourage further exploration of geometrically-aware representation learning in restoration and related areas.

G USE OF LARGE LANGUAGE MODELS (LLMs)

We used OpenAI’s GPT-based Large Language Models (LLMs) (OpenAI, 2023; 2022) to polish the writing and improve the readability of the paper. The models were not used for developing the methodology, running experiments, or analyzing results. All scientific contributions remain entirely the work of the authors.